Universidad de Oviedo

# Electronic Properties in Transition Metal Dichalcogenides

Trabajo de Fin de Máster de la Universidad de Oviedo para obtener el Máster en Física Avanzada: Partículas, Astrofísica, Nanofísica y Materiales Cuánticos

*Presenta: Christian Lanza García*

*Tutor: Jaime Ferrer Rodríguez*

# Contents

## Acknowledges

*I want to thank Jaime Ferrer Rodríguez all the help provided during the first months of these research before the Covid-19 pandemic as well as praise his efforts for this work to continue during the confinement.*

*I also want to thank José Ignacio Martín Carbajo his dedication and devotion to the Master's organization and scheduling and his efforts for its continuity the next promotion. This region needs this Master's degree and he is one of the main responsible persons that ensures this need is fulfilled.*

### Objectives

This research has pursued several goals. A motivation to the research constitutes the first chapter of this work, which has been written looking for a pedagogical result. The necessary knowledge of the basics in topology is part of a dicotomy in which the focus on physics plays the other role. In addition, since a topological field theory approach is out of the scope of this work, a careful analysis on the major features of topology in condensed matter physics and a concise explanation have been pretended to offer the reader a suitable picture. Chapter 2 deals with the basics to understand the main concepts which relate topology with condensed matter physics. A lot of algebra has been computed by the author to obtain almost all the results that appear through the text. Among these calculations, some of them appear in the appendices, but many others are part of pages and pages of personal manuscripts. In example, a lot of time was devoted to obtain the electron dynamics equations with and without magnetic field as well as the same equations under the wave packet approach. Due to the size of these derivations and the fact that a pedagogical focus is pursued, they are omitted in this text.

A third chapter is devoted to show some relevant examples of topological phases. Some others could have been chosen, but the ones in this work are expected to be enough to communicate the main ideas. With a suitable overview, a research in Transition Metal Dichalcogenides (TMDC's) is detailed in Chapter 4. A Tight Binding approach has been performed in order to obtain the band structure, the Berry curvature and the degree of circular polarization in several TMDC's. This is pretended to show the power of these materials as well as their link with topology.

A final research is devoted to the Armchair Graphene Nanoribbons (AGNR's) in Chapter 5. The work that has been developed consists of the study of the band structure of AGNR's depending on the number of dimer lines, as well as a topological characterization through the $\mathbb{Z}_2$ topological invariant. Conclusions to the research are exposed in the last chapter of this text.

# 1 MOTIVATION

In 1980 K.V. Klitzing [1] discovered the Hall conductance quantization in an experiment which determined the hyperfine structure constant in a remarkable accurate fashion. This experiment can be thought as the cornerstone from which latter succesful results were found leading to determine a relation between topology and semiconductor physics [2-8]. A remarkable calculation [3] found a direct relation between topological invariants and the Hall conductance quantization. This computation, though genuine, had a lack of formalism. M. V. Berry's work [8] set a new idea that can be thought as the fundamental theory from which topology can be related to condensed matter physics in a formalized fashion in modern days.

The classification of the states of matter play a fundamental role in physics. In order to stablish a robust classification of the phases of matter, Ginzburg-Landau theory deals with local order parameters which have a finite expectation value in some phase. Landau's theory of phase transitions allows to describe symmetry-broken states through this parameter such as, in example, the overall magnetization in ferromagnets. However, the local nature of the order parameters seems to be insufficient to describe phases in which a local order parameter cannot be defined. Some of these phases which do not have a local order parameter are topological phases in the sense that a topological field theory can describe their low-energy field theory. These phases are described by a non-local order parameter called the topological invariant.

Topology describes manifolds in terms of how they can be deformed. A manifold has a given topology while deformations on it can be performed continuously. Different topologies imply that no continuous deformations can occur between manifolds belonging to each different topological space. Thus, topological invariance is said to happen when a deformation on a manifold can be performed in a continuous fashion, which is also known as homotopy. Two spaces are said to be homotopic if one can be deformed into another without discontinuities. A parameter, called topological invariant, can be set to describe the topology of a system. However, it is not always straight-forward to determine which parameter can define the topology of our system; in fact, this can be a time-consuming issue. A well-known invariant for some physical systems is the so-called $\mathbb{Z}_2$ invariant, which defines a system as trivial (i.e, a conventional insulator) or non-trivial, such as a Topological Insulator (TI). However, this is not always the invariant we need nor the invariant that works properly in order to stablish a topological characterization. At this point, one may ask what is the difference between a topological and a normal system. A first comment must be done: there is no "normal" system, considered as part of a dichotomy between topological and non–topological systems. One can give a topology to any system, and this one can be trivial or non-trivial as well. Conventional insulators and semiconductors have a trivial topology, usually characterized by a $\mathbb{Z}_2 = 0$ invariant, while those that are named as topological phases have a non-trivial topology, described by a $\mathbb{Z}_2 = 1$ invariant (in case this is the useful one). There are several non-trivial (topological) phases; Quantum Hall Effect (QHE), Quantum Spin Hall Effect (QSHE) and TI's are some of them. The physical meaning is that they are protected; this means that, at low energies, perturbations to the system such as deffects or impurities do not modify the phase characteristics since the states of such a system are strong.

These protected states give rise to a new physics which can be implemented in semiconductors business. Spintronics and Valleytronics are two powerful fields to exploit this idiosyncrasy. But how does topology connect with physics? A useful example [9] is the following. Consider an orange such as an ideal sphere. One can deform it continuously into a different object such as an ovoid, but it would not be possible to convert the orange into a doughnut, since a doughnut has a toroidal geometry. However, one could deform the doughnut continuously into, let us say, a cup of coffe. This is also related to the number of holes the geometry has, and has to do with the so-called genus. Gauss and Bonnet stablished a connection between geometry and topology in terms of this genus (the famous Gauss-Bonnet theorem) or the Euler characteristic as well. In the case of the QHE, in example, a result for the Hall conductance quantization will be found, which can be seen conceptually related to this famous theorem. If these deformations are now thought as variations in a parameter space of the hamiltonian, then a continuous variation of its parameters will lead to a different hamiltonian and eigenstates which preserve the same topology. Thus, a hamiltonian describing a phase of matter can have the same topology as another one which has been modified through its internal parameters (continuously and usually in a smooth fashion). In addition it is also possible to find changes that induce a discontinuous variation and so a change in the topological phase classification. This implies a variation in the topology and reflects itself in the hamiltonian, eigenvalues and eigenstates as well. As an example, in the Su-Schrieffer-Heeger model (SSH) a variation in the parameter space through the hopping amplitudes leads to a change in the topology of the system, and, particularly, there are some values for which the transition occurs. This is also true for other models such as Haldane's model or the QSHE. Specifically, this transition regions are characterized by a gap closure, which allows for a non-zero conductance and the appearance of special states known as edge or boundary states depending on the dimensions of the system. These states are strongly protected by symmetries which depend on the system we are studying, and this protected-like behavior endows semiconductor physics with a beautiful paradigm.

Topological-related concepts appear in a natural fashion in Transition Metal Dichalcogenides (TMDC's) due to its lack of inversion symmetry. A non-vanishing Berry curvature at the valleys in the $\pm K$ points of the First Brillouin Zone (1BZ) and the separation between these points which prevents the existence of intervalley scattering allows valley-dependent phenomena to occur if a correctly polarized light is applied, creating interband excitons and a non-zero transverse conductivity.

These issues are also interesting for Graphene Nanorribbons. Graphene's world arose as the cornerstone of 2D materials and the hope placed on this material was related to its room-temperature ballistic electronics, its high electron mobility and its long coherence length. However, graphene-based field-effect transistors (FET) development has experienced a major setback due to its metallic behavior. A suitable option to overcome this problem is to open the band gap in graphene, which can be performed by means of graphene nanoribbons due to its boundary conditions. This is a hot topic that can also be related to topological phases and topological invariant calculations.

# 2 PHYSICS AND TOPOLOGY

The First Brillouin Zone (1BZ) has the topology of a $T^D$ torus in $D$ dimensions. It can be useful to think of a rectangular $2D$ 1BZ and consider the periodicity in both the horizontal and vertical axes. One is then able to join equivalent points (which are those in the horizontal and vertical axes), obtaining a torus. Gauss-Bonet theorem stablishes that the topology of a torus is different from that of a sphere, and it is characterized by the so-called genus, related to the number of holes in the figure. This genus can be thought as a topological invariant of the system, but topological invariants (which are the main tool needed to determine the topology of a system) are not easy to stablish. In order to do so, some concepts must be introduced before. K.V. Klitzing's discovery [1] laid the cornerstone from which topology and physics became closer during the 80's. Later works like those of R. B. Laughlin [2] or D. J. Thouless [3-5] tried to set a formalism for this new physics. But the theoretical cornerstone was set by the work of M. V. Berry [8] on the adiabatic variation of the parameters of the time-dependent Schrödinger equation. He showed that apart from a dynamical phase, a geometrical one appears as a constituent of the solution to the instantaneous eigenstates of a parameter-dependent hamiltonian. Actually, this phase had been known from the beginning of quantum mechanics, but had been supressed since it was considered as artificial [10]. This is the so-called Berry phase, which is also known as Zak's phase in the context of Bloch bands [11]. The connection with topology is readily stablished from this factor, as will be shown latter [12]. In order to obtain this phase, two quantities appear; the Berry connection and the Berry curvature, which are essential to describe the electron dynamics under an electric field (or even a magnetic field). The Berry curvature is also a suitable tool to study the topology of a system, as will be shown. Likewise, the connection between topology and condensed matter physics through the Berry phase also implies a close relationship between topology and valleytronics, since the Berry curvature is a fundamental quantity in the frame of this new physics.

## 2.1 Berry phase, Berry connection and Berry curvature

Let $\hat{H} = \hat{H}(\mathbf{R})$ be a time-dependent hamiltonian through the parameter $\mathbf{R} = \mathbf{R}(t)$. Its eigenvalues and eigenvectors do not have a concrete Hilbert space but an instantaneous one, so they will also depend on this variable through the parameter $\mathbf{R}$. An instantaneous orthonormal basis $|n(\mathbf{R})\rangle$ can be defined. We can set the Schrödinger equation for a system like this as

$$\hat{H}(\mathbf{R})\,|n(\mathbf{R})\rangle = E_n(\mathbf{R})\,|n(\mathbf{R})\rangle \tag{2.1}$$

Eq. (2.1) describes the adiabatic evolution as $\mathbf{R}$ moves slowly along a path $C$ in the parameter space. Since we are allowed to introduce a phase factor, the states $|n(\mathbf{R})\rangle$ are not completely determined. A smoothly variating and single-valued phase along the parameter space is required. The state $|\psi\rangle$ at time $t$ can be built from a linear combination such as

$$|\psi\rangle = \sum_n e^{i\phi_n} c_n \left|n\left(\mathbf{R}\right)\right\rangle \tag{2.2}$$

where a phase factor with $\phi_n = \phi_n(t)$ has been introduced. The phase is described as

$$\phi_n(t) = -\frac{1}{\hbar}\int_{t_o}^{t} E_n\left(\mathbf{R}\right) dt' \tag{2.3}$$

where $\mathbf{R} = \mathbf{R}\left(t'\right)$, and it is called the dynamical phase since it is related to the energy of the system. Another phase-dependent term $c_n = c_n(t)$ has been introduced. This one is known as the geometrical phase term since it depends on the path along the temporal evolution. This term is related to the famous Berry phase [8] and has the following form:

$$c_n = e^{i\gamma_n} \left|c_n\right| \tag{2.4}$$

where $\gamma_n = \gamma_n\left(t\right)$ is the Berry phase. Appendix A.1 is devoted to perform this calculation, which leads to

$$\gamma_n = i\int \left\langle n\left(\mathbf{R}\right)\right| \partial_{t'} \left|n\left(\mathbf{R}\right)\right\rangle dt' \tag{2.5}$$

It is clear that the Berry phase has an implicit dependence on the parameters $\mathbf{R}$ which depend on the path $C$. Taking into consideration

$$\partial_{t'} \left|n\left(\mathbf{R}\right)\right\rangle = \boldsymbol{\partial}_{\mathbf{R}} \left|n\left(\mathbf{R}\right)\right\rangle \dot{\mathbf{R}} \tag{2.6}$$

the expression for the Berry phase through a close loop $C$ can be recast into[1]

$$\gamma_n = i\oint_C \left\langle \psi_n\left(\mathbf{R}\right)\right| \boldsymbol{\partial}_{\mathbf{R}} \left|\psi_n\left(\mathbf{R}\right)\right\rangle d\mathbf{R} = \oint_C \mathbf{A}_n\left(\mathbf{R}\right) d\mathbf{R} \tag{2.7}$$

for a closed loop. We have just introduced a new quantity $\mathbf{A}_n\left(\mathbf{R}\right)$ known as Berry connection or Berry potential. A problem arises since the Berry connection is gauge dependent, as we can see below. After performing a gauge transformation such as

$$\mathbf{A_n}\left(\mathbf{R}\right) \longrightarrow \mathbf{A_n}\left(\mathbf{R}\right) - \boldsymbol{\partial}_{\mathbf{R}}\xi\left(\mathbf{R}\right) \tag{2.8}$$

where $\xi\left(\mathbf{R}\right)$ is the phase of the gauge transformation such that the eigenstates transform as $\left|n\left(\mathbf{R}\right)\right\rangle \longrightarrow e^{i\xi(\mathbf{R})}\left|n\left(\mathbf{R}\right)\right\rangle$, we get the following transformation for the Berry phase:

$$\gamma_n \longrightarrow \gamma_n - \left[\xi\left(\mathbf{R}\right) - \xi\left(\mathbf{R}_0\right)\right]. \tag{2.9}$$

In the case of a closed path, due to the monovaluated character of the basis functions ($\left|n\left(\mathbf{R}\right)\right\rangle = \left|n\left(\mathbf{R}_0\right)\right\rangle$), the following condition must be satisfied:

[1] Notice that for $\dot{\mathbf{R}} \longrightarrow 0$, the Berry phase goes to zero, which implies that the coefficient for the n-th eigenstate is constant.

$$\xi(\mathbf{R}) - \xi(\mathbf{R}_0) = 2\pi n, n \in \mathbb{N} \tag{2.10}$$

Thus, although the Berry connection is gauge dependent, the integral in eq. (2.7) will be gauge invariant; and so the exponential in the phase term $c_n$. The fact that $\xi(\mathbf{R}) - \xi(\mathbf{R}_0)$ is non-zero implies that the Berry phase cannot be removed[2]. In analogy to the stress-energy tensor $F^{\mu\nu}$ in the context of electrodynamics, we are able to define a new tensor derived from the Berry connection as

$$\Omega^n_{\mu\nu}(\mathbf{R}) = \partial_\mu A^n_\nu - \partial_\nu A^n_\mu \tag{2.11}$$

This tensor is known as Berry curvature[3]. A further expression can be given for this tensor as

$$\Omega^n_{\mu\nu}(\mathbf{R}) = i\left[\left\langle \partial_\mu n(\mathbf{R}) \left| \partial_\nu n(\mathbf{R}) \right\rangle - \left\langle \partial_\nu n(\mathbf{R}) \left| \partial_\mu n(\mathbf{R}) \right\rangle \right.\right] \tag{2.12}$$

We can write it as a vector through the following vectorial product:

$$\boldsymbol{\Omega^n}(\mathbf{R}) = \boldsymbol{\partial}_{\mathbf{R}} \times \mathbf{A_n}(\mathbf{R}) \tag{2.13}$$

Eq. (2.13) allows to write the Berry phase in terms of the Berry curvature vector by applying Stoke's theorem as follows:

$$\gamma_n = \oint_C \mathbf{A_n}(\mathbf{R})\, d\mathbf{R} = \int_S (\boldsymbol{\partial}_{\mathbf{R}} \times \mathbf{A_n}(\mathbf{R}))\, d\mathbf{S} = \int_S \boldsymbol{\Omega^n}(\mathbf{R})\, d\mathbf{S} \tag{2.14}$$

This curvature vector can be seen as an effective magnetic field in the parameter space (think of electrodynamics and the relation between the magnetic field and the magnetic potential).

There is a different approach to write $\Omega^n_{\mu\nu}(\mathbf{R})$ (see Appendix A.2):

$$\Omega^n_{\mu\nu}(\mathbf{R}) = i \sum_{n' \neq n} \left[ \frac{\langle n(\mathbf{R}) | \partial_\mu H(\mathbf{R}) | n'(\mathbf{R}) \rangle \langle n'(\mathbf{R}) | \partial_\nu H(\mathbf{R}) | n(\mathbf{R}) \rangle - c.c}{(E_n - E'_n)^2} \right] \tag{2.15}$$

Eq. (2.15) is an alternative way to write the Berry curvature in terms of the derivatives of the hamiltonian, which has been proven to be much more efficient in numerical calculations.

## 2.2 Degeneracies and the Berry curvature

The Berry curvature is a local quantity since it provides a local description of the geometric properties of the parameter space [10]. In addition, it is shown that the Berry curvature vanishes for each value of $\mathbf{R}$ as follows:

[2] Fock (1928) argued to choose a $\xi(\mathbf{R})$ such that the phase gets cancelled at the end of the loop. This implied to delete this phase term since it was seen as an artificial factor. However, Berry's work [8] showed that considering a non-vanishing phase had deep physical consequencies.

[3] This quantity has played a crucial role in the work performed on the electronic properties of TMDC's materials.

$$\sum_n \Omega^n_{\mu\nu}(\mathbf{R}) = 0 \tag{2.16}$$

The sum runs over the number $n$ of filled bands. This equation proves the local conservation law for the Berry curvature. It is also seen that a singularity appears if two energy levels coincide for a same $\mathbf{R}$, this is, if they are degenerate. The classification of degeneracies is one the most relevant applications of Berry's work, being a crucial tool in topological band theory. This situation where a singularity appears corresponds to a monopole in the parameter space [10]. In order to explain it, let us set a 2-band parameter-dependent hamiltonian $H = H(\mathbf{R})$ such that

$$H(\mathbf{R}) = \mathbf{h} \cdot \boldsymbol{\sigma} \tag{2.17}$$

with $\mathbf{h} = h\,(sin\theta cos\phi, sin\theta sin\phi, cos\theta)$. A straightforward calculation leads to

$$H = \begin{pmatrix} h_z & h_x - ih_y \\ h_x + ih_y & -h_z \end{pmatrix} \tag{2.18}$$

whose eigenvalues are $\lambda^{\pm} = \pm\sqrt{h_x^2 + h_y^2 + h_z^2}$. The conduction and valence band eigenvectors are found to be

$$\begin{pmatrix} u^+ \\ v^+ \end{pmatrix} = \begin{pmatrix} cos\left(\frac{\theta}{2}\right) \\ sin\left(\frac{\theta}{2}\right) e^{i\phi} \end{pmatrix} \tag{2.19}$$

$$\begin{pmatrix} u^- \\ v^- \end{pmatrix} = \begin{pmatrix} sin\left(\frac{\theta}{2}\right) e^{-i\phi} \\ -cos\left(\frac{\theta}{2}\right) \end{pmatrix} \tag{2.20}$$

being orthonormal to each other. It can be seen that for the valence band there is a singularity if $h_z + |\mathbf{h}| = 0$, which is satisfied if $\theta = \pi$. In addition, a singularity appears in the conduction band eigenvector when $h_z - |\mathbf{h}| = 0$, this is, if $\theta = 0$. Thus, the wavefunctions are not well-defined on the whole Bloch sphere. One is able to add a gauge factor to, let us say, the valence band, in order to fix its singularity at the south pole of the sphere. In fact, this gauge transformation changes the Berry connection but leaves the Berry curvature invariant. This allows to confirm that the Berry curvature is gauge-invariant. After some algebra one can obtain the Berry curvature for the valence and the conduction band:

$$\boldsymbol{\Omega}_{\boldsymbol{v(c)}} = +(-)\frac{1}{2}\frac{\mathbf{h}}{h^3} \tag{2.21}$$

The previous equation is analogous to the field generated by a monopole at the origin, where the 2 bands are degenerate, which shows that the degeneracy points ($h = 0$) are sources and drains of the Berry curvature [10]. If an integration over the whole sphere containing the monopole is performed, a factor $2\pi$ is obtained. If the integration is performed over a different closed manifold containing a number $n$ of monopoles, then the result wil be $2\pi n$. In the context of Chern insulators (discussed in Chapter 3), since we are not able to find a gauge that fixes the

singularities of both wavefunctions, a non-zero Hall conductance can appear. The $n$ number is, in the context of Chern insulators, the Chern number.

## 2.3 Electron dynamics under adiabatic perturbations

One can obtain that a first-order approximation of the eigenstates of a general hamiltonian $H(\mathbf{R})$ can be written as[4]

$$|\psi\rangle = e^{-\frac{i}{\hbar}\int_{t_o}^{t} E_n dt'} \left[ |n\rangle - i\hbar \sum_{n \neq n'} \frac{|n'\rangle \langle n'| \partial_t n\rangle}{E_n - E_{n'}} \right] \tag{2.22}$$

Since we are interested in Bloch states such that

$$\left|\psi_{n\mathbf{k}}(\mathbf{r})\right\rangle = e^{i\mathbf{kr}} \left|u_n(\mathbf{k},t)\right\rangle \tag{2.23}$$

one can consider the periodic part of a Bloch state and apply eq. (2.22) on it:

$$\left|u_n(\mathbf{k},t)\right\rangle \longrightarrow \left|u_n(\mathbf{k},t)\right\rangle - i\hbar \sum_{n \neq n'} \frac{|u_{n'}(\mathbf{k},t)\rangle \langle u_{n'}(\mathbf{k},t)| \partial_t u_n(\mathbf{k},t)\rangle}{E_n - E_{n'}} \tag{2.24}$$

up to a factor $e^{-\frac{i}{\hbar}\int_{t_o}^{t} dt' E_n(t')}$. On the other hand, it is well-known that the velocity operator in the real space is defined by $\hat{v} = \frac{i}{\hbar}\left[\hat{H}, \hat{r}\right]$, which can be written in the $\mathbf{k}$-space by just performing an unitary transformation such that

$$\hat{v}(\mathbf{k}) = e^{-i\mathbf{kr}} \frac{i}{\hbar} \left[\hat{H}, \hat{r}\right] e^{i\mathbf{kr}} \tag{2.25}$$

which is the same that

$$\hat{v}(\mathbf{k}) = \frac{1}{\hbar} \partial_{\mathbf{k}} \hat{H}(\mathbf{k},t) \tag{2.26}$$

The calculation performed in Appendix A.3 allows to obtain the expectation value of the velocity operator in the first-order perturbated basis $\{\left|u_n'(\mathbf{k},t)\right\rangle\}$ (which is our new basis):

$$\dot{\mathbf{r}} = \frac{1}{\hbar} \partial_{\mathbf{k}} \mathbf{E_n}(\mathbf{k}) - \Omega_{\mathbf{k}t}^{n} \tag{2.27}$$

Two important cases shall be studied, which are the perturbations through a weak electric field $\mathbf{E}$ and a more general case where both electric and magnetic field are present. The addition of an electric field implies the existence of an electrostatic potential whose dependence on $\mathbf{r}$ makes the translational symmetry to be broken in the context of Bloch's theorem. In order to overcome this symmetry rupture one can use Peierls substitution and introduce the electric field considering a gauge tranformation from real space to a $\mathbf{q}$-space by a gauge transformation such that $\mathbf{k} = \mathbf{k}(\mathbf{q},t)$ by $\mathbf{k} = \mathbf{q} + \frac{e}{\hbar}\mathbf{A}(t)$, where $\mathbf{A}(t)$ is the gauge potential that introduces the electric

[4] See Appendix A.1.

field as $\mathbf{E} = -\partial_t \mathbf{A}(t)$ and $\mathbf{k}$ is the gauge-invariant crystal momentum. If, as it has been stated, the gauge potential only depends on time, it preserves translational symmetry, which implies that $\mathbf{q}$ is a constant of motion such that $\dot{\mathbf{q}} = 0$. Then one finds that $\dot{\mathbf{k}} = -\frac{e}{\hbar}\mathbf{E}$. A tedious algebra has to be computed in order to obtain the following result. Due to the size of this calculus, it is omitted in this text[5]. An equation for the velocity is presented below:

$$\dot{\mathbf{r}} = \frac{1}{\hbar}\partial_{\mathbf{k}}\mathbf{E}_{\mathbf{n}}(\mathbf{k}) - \frac{e}{\hbar}\mathbf{E} \times \boldsymbol{\Omega}_{\boldsymbol{n}}(\mathbf{k}) \tag{2.28}$$

In addition to the usual term, a new one arises from the preceeding perturbative treatment, which corresponds to the famous anomalous velocity. This velocity is transverse to the electric field ensuring the appearance of a Hall current (see later chapter)[6]. A more general result can be obtained considering the semiclassical dynamics of the electrons in magnetic Bloch bands [13,14]:

$$\dot{\mathbf{r}} = \frac{1}{\hbar}\partial_{\mathbf{k}}\boldsymbol{\varepsilon}_{\mathbf{n}}(\mathbf{k}) - \dot{\mathbf{k}} \times \boldsymbol{\Omega}_{\boldsymbol{n}}(\mathbf{k}) \tag{2.29}$$

$$\hbar\dot{\mathbf{k}} = -e\mathbf{E} - e\dot{\mathbf{r}} \times \mathbf{B}(\mathbf{r}) \tag{2.30}$$

An orbital magnetic moment can be defined as

$$\mathbf{m}(\mathbf{k}) = -i\frac{\hbar^2}{2m^2}\sum_{n' \neq n}\frac{\mathbf{P}^{nn'}(\mathbf{k}) \times \mathbf{P}^{n'n}(\mathbf{k})}{E_{n'}(\mathbf{k}) - E_n(\mathbf{k})} \tag{2.31}$$

where $\mathbf{P}^{nn'}(\mathbf{k}) = \langle u_{n\mathbf{k}} | \hat{v}(\mathbf{k}) | u_{n\mathbf{k}} \rangle$ is the matrix element of the velocity operator. For a null magnetic field, the previous equations reduce to the ones in the weak electric field perturbation case straight-forwardly. It must be pointed out that the energy is not the one in eq. (2.28) but $\varepsilon_n(\mathbf{k}) = E_n(\mathbf{k}) - \mathbf{m}(\mathbf{k})\mathbf{B}(\mathbf{r})$. A correction due to the orbital magnetic moment appears[7] [13,14]. The anomalous velocity gives rise to the Hall conductivity in ferromagnets.

Symmetries have a crucial influence on the Berry curvature, and thus on the topology of the system. Systems with different symmetries will be considered in the next chapter, and depending on them, different topological phases arise. It is remarkable that systems with both parity and time-reversal symmetries have a vanishing Berry curvature, since $\boldsymbol{\Omega}(\mathbf{k}) = \boldsymbol{\Omega}(-\mathbf{k})$ (parity) and $\boldsymbol{\Omega}(\mathbf{k}) = -\boldsymbol{\Omega}(-\mathbf{k})$ (time-reversal) have to be simultaneously satisfied. A null Berry curvature is characteristic of topologically trivial systems. However, when one of these symmetries is broken, the Berry curvature has a non-zero value over some point in the 1BZ, even although it is globally null[8]. Particularly, a system which preserves only time-reversal symmetry may have different values of the Berry curvature at each $\mathbf{k}$ in the 1BZ, while the integral over this 1BZ of this curvature remains zero. Conversely, a system which only preserves inversion symmetry may have,

[5] In fact, it is easier to go backwards from the result in order to obtain the left-hand-side terms.

[6] Another approach can be followed to obtain eq. (2.28), the so-called wave packet formalism.

[7] An important work was developed in the 90's using the wave packet approach. In fact, the previous equations where obtained this way.

[8] This is the case of TMDC's.

in addition to the locally non-zero values of the Berry curvature, a non-zero value of the integral of the Berry curvature over the 1BZ. A phase with both broken inversion and time-reversal symmetries is the QSHE in graphene [15-17]. Phases with broken inversion symmetry (preserving time-reversal symmetry) are particularly of interest for our purposes, since valleytronics arises in this context. The orbital magnetic moment also arises from this broken inversion symmetry[9]. Note that $\mathbf{P}^{nn'}(\mathbf{k})$ in eq. (2.31) is also related to the degree of optical polarization [18,20]. The Berry curvature can be also formulated in terms of these matrix elements [19,21].

## 2.4 Time-reversal symmetry (TRS) and $\mathbb{Z}_2$ invariant

Time-reversal symmetry (TRS) is crucial for topological condensed matter since materials with time-reversal invariance are experimentally realizable. Systems which are not time-reversal (TR) invariant may exhibit Hall voltages or other interesting physics. However, although TR invariant systems do not display Hall effects, they are able to show other topologically-related properties related to the $\mathbb{Z}_2$ invariant.

Spinless particles and spinful particles have different TR operators. The TR operator is usually defined as $\hat{T} = UK$ where $U$ is a unitary matrix and $K$ is the complex conjugation operator[10]. For spinless particles, the $U$ matrix has no deep importance since $U = U^T$, condition which guarantees that $\hat{T}^2 = +1$. The time evolution operator $\hat{T}$ is antiunitary and its action on the Bloch bundle[11] behaves as a map connecting fibers in $k$ with fibers in $-k$ as[12]

$$\hat{T}h(k)\hat{T}^{-1} = h(-k) \tag{2.32}$$

which means that for an eigenstate $|u_n(k)\rangle$, $\hat{T}|u_n(k)\rangle$ is an eigenstate at $-k$. In addition, for spinless particles no double degeneracy is necessary at the time-reversal invariant momentum points (TRIM), since $\langle u_i(k)|\hat{T}|u_j(k)\rangle \neq 0$. This means that both wavevectors can belong to the same band. In fact, for spinless particles, a 1-band system can be a suitable option.

A different physics arise when dealing with the spin. As an angular momentum, it must obey $\hat{T}\mathbf{S}\hat{T}^{-1} = -\mathbf{S}$, which describes a spin direction flipping. This allows to represent the TR operator as (apart from the conjugation) a rotation around an arbitrary axis. Choosing the $y$ axis a general result can be obtained:

$$= e^{-i\pi S_y}K \tag{2.33}$$

[9] The Berry curvature has also an effect on the phase-space volume and thus on the electron density of states [10]. However, this is not crucial for this work, so this will not be adressed.

[10] The presence of the $K$ operator is readily found necessary from the TR transformation of $[\hat{x},\hat{p}]$. Note that $T\hat{x}T^{-1} = \hat{x}$ while $T\hat{p}T^{-1} = -\hat{p}$.

[11] As mentioned previously, 1BZ has a toroidal topology, which makes the 1BZ to be known as Brillouin torus $T^d$ for $d-$dimensions. For each $\mathbf{k}$ there exists a Bloch hamiltonian $\hat{H}(\mathbf{k})$ related to a infinite dimensional Hilbert space that can be represented as $H_{\mathbf{k}}$. A bloch bundle is a fiber bundle such that

$$\pi : H_{\mathbf{k}} \longrightarrow T^d$$

[12] This stands for both spinless and spinful particles.

Calculating twice the TR operator a fundamental result is found:

$$\hat{T}^2 = e^{-i2\pi S_y} \tag{2.34}$$

Note that for integer spin particles, twice the action of the TR operator over a wavefunction describes a $2\pi$ rotation, which is equivalent to the identity operator. However, half-integer spin particles experiment a $\pi$ rotation, which gives a factor $\hat{T}^2 = -1$. Performing the exponential of $-i\pi S_y$ with $S_y = \frac{\sigma_y}{2}$ the following formula for the TR operator is obtained:

$$\hat{T} = -i\sigma_y \hat{K} \tag{2.35}$$

Because of antiunitarity, it fulfills $\hat{T}^2 = -1$. Since this condition must be satisfied, eigenvalues of $|u_k\rangle$ and $\hat{T}|u_k\rangle$ have to be different; otherwise $\hat{T}^2|u_k\rangle = |u_k\rangle$. In fact, they are distinct but have the same energy. This result is remarkable and is known as Kramer's degeneracy. For a TR invariant hamiltonian, $[\hat{H}, \hat{T}] = 0$ and then $|u_k\rangle$ and $\hat{T}|u_k\rangle$ are eigenstates of the hamiltonian. In addition, they are orthogonal since $\langle u_k|\hat{T}|u_k\rangle = 0$. We can also prove that the scattering probability of the state $|u_k\rangle$ into its partner $\hat{T}|u_k\rangle$ is

$$\left\langle \hat{T}u_k \right| \hat{H}|u_k\rangle = -\left\langle \hat{T}u_k \right| \hat{H}|u_k\rangle = 0 \tag{2.36}$$

It can be thought as an energy degeneration $E(\mathbf{k}) = E(-\mathbf{k})$ for the hamiltonian bundles so that the energy for $|u_k\rangle$ and $|u_{-k}\rangle$ is the same, which results in a bundle double degeneracy at some points of the Brillouin torus, the so-called Time Reversal Invariant Momenta (TRIM).

For a single-band below the Fermi energy in a spinless system we can obtain that the Berry curvature behaves as $\Omega_{\mu\nu}(-k) = -\Omega_{\mu\nu}(k)$, which leads to a vanishing value upon integration over the 1BZ. The same can be obtained for a spinful system[13].

Kramer's pairs fulfill

$$E(\mathbf{k}) = E(-\mathbf{k}) \tag{2.37}$$

which implies that they have the same energy for opposite $\mathbf{k}$. A cornerstone example is graphene with spin-orbit coupling (SOC)[14]. These Kramer's pairs are formed by the so-called edge states. The number of Kramer's pairs is related to the topological invariant of the phase. It must be pointed out that Chern's number for a TRS model is zero, since each band's Chern's number can only be

$$C_{\uparrow(\downarrow)} = +(-)1 \tag{2.38}$$

and the total Chern's number is the sum of all of them. This is a good moment to introduce the previously mentioned $\mathbb{Z}_2$ invariant. For the case of a TRS system, this can be defined (in terms

[13] This is crucial to understand why TR invariant systems cannot exhibit a non-zero Hall conductance.
[14] See later chapters.

of the Chern's total number) as

$$\mathbb{Z}_2 = \frac{C_\uparrow - C_\downarrow}{2} mod(2) \tag{2.39}$$

and it can take values 0 or 1, depending on the number of Kramer's pairs (this is, if it is even or odd respectively). One can also relate the invariant to the number of Kramer's pairs as

$$\mathbb{Z}_2 = N mod\,(2) \tag{2.40}$$

Although this is an important result, a general vision on the $\mathbb{Z}_2$ invariant is prefered to be presented related to a general symmetry. There is a lot of work developed to compute $\mathbb{Z}_2$ invariants for physical systems [9,15-17,22]. Two remarkable approaches are of theoretical interest. The first method to calculate a $\mathbb{Z}_2$ invariant[15] is from the Time Reversal Polarization (see Appendix A.4). It is defined as

$$P_\theta = \frac{1}{i\pi} ln \left[ \frac{w\,(\pi)}{w\,(0)} \frac{\sqrt{w^2\,(0)}}{\sqrt{w^2\,(\pi)}} \right] \tag{2.41}$$

where $w$ is the matrix representation of the time-reversal operator. We can rewrite the Time Reversal Polarization as

$$(-1)^{P_\theta} = \frac{\sqrt{det\,[w\,(0)]}}{Pf\,[w\,(0)]} \frac{\sqrt{det\,[w\,(\pi)]}}{Pf\,[w\,(\pi)]} \tag{2.42}$$

This result can be generalized to a torus (the 1BZ) in which the 4 TRIM are considered:

$$(-1)^{\mathbb{Z}_2} = \prod_{i=1}^{4} \frac{Pf\,[w\,(\Lambda_i)]}{\sqrt{det\,[w\,(\Lambda_i)]}} \tag{2.43}$$

which is appropiate for a $2D$ system.

A different approach is to consider that enforcing the time reversal constraint implies a $\mathbb{Z}_2$ invariant to be an obstruction such that the gauges for wavefunctions at $\pm\,(k,t)$ are not independent. Considering the four TRIM, a transformation such as $|u_{k,n}\rangle \longrightarrow \sum_m U_{nm}\,(k)\,|u_{k,m}\rangle$ has to be symplectic. A non-zero $\mathbb{Z}_2$ invariant is not consistent with the constraint since thus $Det\,(w\,(k,t)) = 1 \forall k,t$ and $Pf\,[w\,(\Gamma_i)] = 1$, which gives $(-1)^{\mathbb{Z}_2} = 0$ in eq. (2.43). A formula for the $\mathbb{Z}_2$ invariant as an obstruction to the constraint is given below in terms of the Berry connection and the Berry curvature. In order to do so one has to guess wavefunctions defined smoothly on two patches A and B in the 1BZ:

[15] Since $\mathbb{Z}_2$ calculations may be different depending on the system, two different approaches have been used in this work. A numerical method is employed in order to obtain the $\mathbb{Z}_2$ invariant in TMDC's, while a symmetry-based approach has been used in AGNR's.

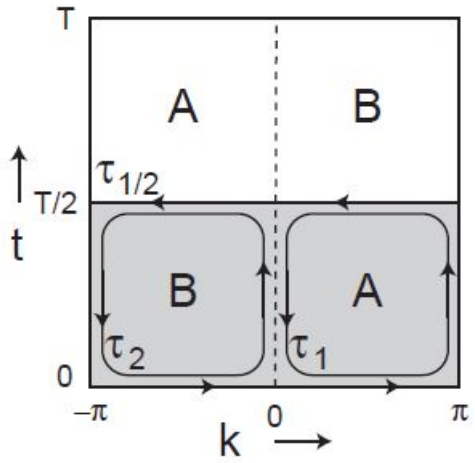


Figure 1: *1BZ torus and patches A and B are shown. $\tau_1$ is the boundary of the A region, while $\tau_2$ is the boundary of B. A boundary $\tau_{1/2}$ is the one of the shaded region.*

We are able to define wavefunctions for regions A and B such that they are related at the overlapping regions by a $U(2N)$ transition matrix $U^{AB}$. Then a change in the $U(1)$ phase of this matrix can be defined around a closed loop $\partial\tau_1$ as

$$D = \frac{1}{2\pi i}\oint_{\partial\tau_1} Tr[U^{AB\dagger}\boldsymbol{\partial} U^{AB}]dl = \frac{1}{2\pi}\oint_{d\tau_1}\left[A^B - A^A\right]dl \tag{2.44}$$

which can be related to the Berry flux by Stoke's theorem:

$$\oint_{\partial\tau_1} A^A dl = \int_{\tau_1} F^A d\tau \tag{2.45}$$

Wavevectors of B are not necessarily well-defined in A, but the can be related to the Berry flux as follows:

$$\oint_{d\tau_1} A^B dl = -\oint_{\partial\tau_2} A^B dl + \oint_{\partial\tau_{1/2}} A^B dl = -\int_{\tau_2} F^B d\tau + \oint_{\partial\tau_{1/2}} A^B dl \tag{2.46}$$

A final result is given:

$$D = \frac{1}{2\pi}\left[\oint_{\partial\tau_{1/2}} A dl - \int_{\tau_{1/2}} F d\tau\right] mod\,(2) \tag{2.47}$$

The final result in eq. (2.47) is the basis of the calculations performed in order to obtain the topological invariant in TMDC's.

# 3 TOPOLOGICAL PHASES

In order to understand the nature of topological materials it is compulsory to consider that, though there are topologically trivial models, this does not imply that their behaviour cannot be related to some kind of trivial topology. This chapter is devoted to study some remarkable systems whose features are related with non-trivial topologies and topological phases. These ones are the Quantum Hall Effect (QHE), the Su-Schrieffer-Heeger model (SSH), Haldane's model and the Quantum Spin Hall Effect (QSHE). The first section is devoted to motivate the study of QHE systems and its relation with the Berry potential and curvature, as well as the characterization of its topological invariant. The second section, devoted to the SSH model, shows how edge states appear and bulk-edge correspondence adquire a major importance. A third section shows the features of Haldane's model, from a graphene system with both inversion and time-reversal symmetries to a system with both of them broken. Haldane's model is essential to understand the QSHE, which is studied in the fourth section. QSHE sets the framework in order to study TI's. The calculation of the $\mathbb{Z}_2$ and its relation to QSHE is also detailed.

## 3.1 Quantum Hall Effect (QHE)

The QHE is quite important for this purpose since, historically, its study lead to a first attemp to unify topological issues with condensed matter physics [2,3,6,7]. Its relation to the QSHE is also a strong reason to deeply study it.

Focusing in $2D$ systems, the classical Hall Effect (HE) lies on the emergence of an electric field (thus, a voltage) in a conductor plane due to a charge polarization when a magnetic field is applied perpendicular to the plane. The HE introduces a tensorial representation for the Ohm's law $j = \sigma E$ where $\sigma$ is a $3 \times 3$ tensor with $\sigma_{ii} = \frac{nq^2\tau}{m}$ and

$$\sigma_{12} = \sigma_{21} = \frac{nq}{B} \tag{3.1}$$

are the non-zero elements. These components of the conductivity tensor are described in terms of the electron concentration $n$, charge $q$ and mass $m$, as well as the relaxation time $\tau$ and the applied magnetic field $B$. The term $\sigma_{ii}$ is known as Drude conductivity an is usually denoted by $\sigma_D$. In the HE another component $\sigma_{12}$ appears, known as Hall conductivity and usually written as $\sigma_H$. This Hall conductivity (or the resistivity, since $\sigma_H = \rho_H^{-1}$) takes continuous values in the HE.

However, when we work on the QHE, the experimental observations conclude that the Hall resistivity is quantized, as studied by [1].

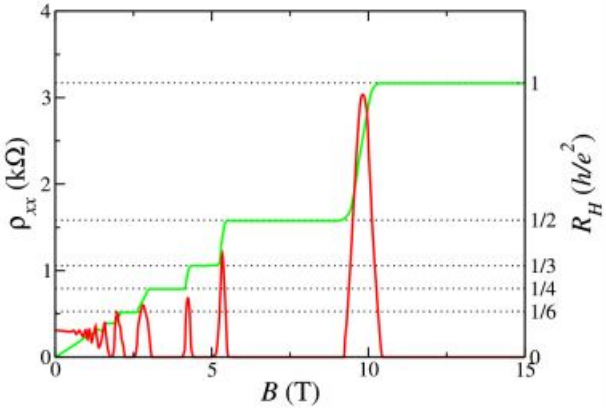


Figure 2: *Longitudinal and transverse resistivity measurements for the QHE. It is observed that while the longitudinal resistivity can be aproximated as a delta function, the transverse component is a constant piecewise-defined function. This quantization is one of the most important features of the QHE and a historically remarkable result which opened a new workline at the beginning of the 80's [1,3,4]. Image created by D.R. Leadley, Warwick University (1997).*

Figure 2 shows a non-linear relation between the resistivity components and the magnetic field in a high magnetic fields domain. This is also true for low temperatures as well. In order to obtain an analytical result for the Hall conductivity a perturbative method is applied below.

Let us focus on a free electron hamiltonian with a source of perpendicular magnetic field **B**. A non-perturbative treatment is shown in Appendix B.1. However, one can also perform a different approach by doing perturbation theory. In order to do so, let us guess a perturbative model in which a perturbation $V = -eEy$ is applied to a fundamental hamiltonian $H_o$. Denoting its eigenstates by $\{|n\rangle\}$, we can define the eigenstates of the perturbated hamiltonian $H = H_0 + V$ as follows from first-order perturbation theory like

$$|n'\rangle = |n\rangle + \sum_{m \neq n} \frac{\langle m| - eEy\,|n\rangle}{E_n - E_m} |m\rangle \tag{3.2}$$

Since the main goal is to compute the expectation value for the current density on the $x$ axis, the following calculus is performed. Note that a Fermi-Dirac distribution function $f(E_n)$ has to be introduced for a finite-temperature system:

$$< J'_x >= \langle n'|\, J'_x\, |n'\rangle = \frac{1}{L^2} \sum_n f(E_n) \langle n'|\, ev_x\, |n'\rangle =$$

$$=< J_x > + \sum_{n,m \neq n} f(E_n) \frac{\langle m| - eEy\,|n\rangle}{E_n - E_m} \langle n|\, ev_x\, |m\rangle +$$

$$+ \sum_{n,m \neq n} f(E_n) \frac{\langle n| - eEy\,|m\rangle}{E_n - E_m} \langle m|\, ev_x\, |n\rangle \tag{3.3}$$

Given that the expectation value for the current density has to be zero for $E = 0$, we need $\langle J_x \rangle$ to be zero too since it is the non-perturbative term. Considering also that

$$\langle m| y |n\rangle = i\hbar \frac{\langle m| v_y |n\rangle}{E_n - E_m} \tag{3.4}$$

one obtains the following:

$$\left\langle J_x^{'} \right\rangle = \frac{-i\hbar e^2 E}{L^2} \sum_n f(E_n) \sum_{m \neq n} [B_{m,n}] \tag{3.5}$$

where

$$B_{m,n} = \frac{\langle m| v_y |n\rangle \langle n| e v_x |m\rangle}{(E_n - E_m)^2} - \frac{\langle n| v_y |m\rangle \langle m| e v_x |n\rangle}{(E_n - E_m)^2} \tag{3.6}$$

In order to obtain the previous expression in momentum space for a periodic lattice, one can take $\{|u_{n\mathbf{k}}\rangle\}$ wavefunctions. Given that $y = i\partial_{k_y}$ in momentum space, the expectation value for the current density can be rewritten as follows:

$$\left\langle J_x^{'} \right\rangle = \frac{-ie^2 E}{\hbar L^2} \sum_{n,\mathbf{k}} f(E_{n\mathbf{k}}) \sum_{m \neq n} \left[ \langle u_{m\mathbf{k}'}| \partial_{k_y} |u_{n\mathbf{k}}\rangle \langle u_{n\mathbf{k}}| \partial_{k_x} |u_{m\mathbf{k}'}\rangle - m \longleftrightarrow n \right] \tag{3.7}$$

which clearly stands for

$$\frac{-e^2 E}{\hbar L^2} \sum_{n \neq m} \sum_{\mathbf{k}} f(E_{n\mathbf{k}}) \left[ \partial_{k_x} A_{ny} - \partial_{k_y} A_{nx} \right] \tag{3.8}$$

where $\left[ \partial_{k_x} A_{ny} - \partial_{k_y} A_{nx} \right] = \Omega_{nz}(\mathbf{k})$. Thus the final result is obtained:

$$\frac{-e^2 E}{\hbar L^2} \sum_{n \neq m} \sum_{\mathbf{k}} f(E_{n\mathbf{k}}) \Omega_{nz}(\mathbf{k}) \tag{3.9}$$

The density current is found to depend on the Berry curvature $\Omega_{nz}(\mathbf{k})$ for the $n$-th band in a vectorial representation. Note that $A_{nj} = i \langle u_{n\mathbf{k}}| \partial_{k_j} |u_{n\mathbf{k}}\rangle$ is the Berry potential. Since the sum (or the integration) of the Berry curvature in the whole 1BZ has to be a constant, we are allowed to write the current density as

$$\left\langle J_x^{'} \right\rangle = \frac{e^2 E}{\hbar} \nu \tag{3.10}$$

From the definition of $J_x$ one gets

$$\sigma_{xy} = \frac{e^2}{\hbar} \nu \tag{3.11}$$

This is the same result obtained without perturbation theory for the Hall conductivity of the QHE. It can be observed that the integral along the whole 1BZ over the filled bands of the Berry curvature gives rise to a number $\nu$ known as the TKNN invariant (Thouless, Kohmoto,

Nightingale y den Nijs) [3]. This result is analogous to the Gauss-Bonet theorem in topology for a band model, which shows the relation between condensed matter physics and topology.

### 3.1.2 Chern number

Since the 1BZ is a torus, it has no boundary. This implies that applying Stoke's theorem to calculate the Berry curvature integral along the 1BZ by performing the integral of the Berry potential (which is supossed to be well-defined) through the boundary $\partial BZ$ will carry to a zero Hall conductivity. A non-zero Hall conductivity appears only if the Berry potential has any singularity at some point in the 1BZ (as in the Bloch sphere monopole case), which is a consequence of the fact that no global gauge can be obtained over the entire 1BZ Thus, a non-zero Chern number can be seen as an obstruction to the application of Stoke's theorem over the whole 1BZ.

Since a non-zero Hall conductivity is related to a non-zero Chern number, the may be some cases for which, through a $U(1)$ gauge transformation $e^{i\xi(\mathbf{k})}$ such that $\mathbf{A_n}(\mathbf{k}) \longrightarrow \mathbf{A_n}(\mathbf{k}) - \boldsymbol{\partial}_{\mathbf{k}}\xi(\mathbf{k})$, the Berry potential is not well-defined. Consider that the wavefunction of the $n$-th energy level can be transformed as

$$|u_{1n}(\mathbf{k})\rangle \longrightarrow e^{i\xi(\mathbf{k})}|u_{1n}(\mathbf{k})\rangle \tag{3.12}$$

We are able to define a different gauge for the points where the singularities appear, considering a small region around them on which

$$|u_{2n}(\mathbf{k})\rangle \longrightarrow e^{i\gamma(\mathbf{k})}|u_{1n}(\mathbf{k})\rangle \tag{3.13}$$

is well-defined. Particularly at the boundary between the different regions, the wavefunctions are related by the following gauge transformation:

$$|u_{2n}(\mathbf{k})\rangle = e^{i\chi(\mathbf{k})}|u_{1n}(\mathbf{k})\rangle \tag{3.14}$$

where $\chi(\mathbf{k}) = \gamma(\mathbf{k}) - \xi(\mathbf{k})$. This allow to relate the Berry potentials of the different wavefunctions as

$$\mathbf{A_2}(\mathbf{k}) = \mathbf{A_1}(\mathbf{k}) + \mathbf{i}\boldsymbol{\partial}_{\boldsymbol{k}}\chi(\mathbf{k}) \tag{3.15}$$

Since the Hall conductivity is an observable quantity, it must be gauge invariant. Then we should have smoothly differentiable wavefunctions in order to compute the Hall conductivity through the integration of the Berry curvature $\boldsymbol{\partial}_{\boldsymbol{k}} \times \mathbf{A}(\mathbf{k})$. With the previous gauges, this can be achieved by patches as follows. Denoting the boundary points of the 1BZ where the $u_{1n}$ wavefunction is well defined as $\partial BZ_1$ and the rest by $\partial BZ_2$, we have

$$\sigma_{xy} = \frac{e^2}{h2\pi i}\left[\int_{\partial BZ_1} A_1(\mathbf{k})\, d\mathbf{k} + \int_{\partial BZ_2} A_2(\mathbf{k})\, d\mathbf{k}\right] \tag{3.16}$$

Since the Brillouin torus does not have a boundary, $\partial BZ_1 = -\partial BZ_2$, which implies opposite orientation. This allows to write the conductivity as

$$\sigma_{xy} = \frac{e^2}{h2\pi i} \oint_{\partial BZ_2} \left[A_2(\mathbf{k}) - A_1(\mathbf{k})\right] d\mathbf{k} \tag{3.17}$$

which is clearly

$$\sigma_{xy} = \frac{e^2}{h2\pi i} \oint_{\partial BZ_2} \boldsymbol{\partial_k} \chi(\mathbf{k})\, d\mathbf{k} \tag{3.18}$$

The Chern number is finally defined as

$$n = \frac{1}{2\pi} \oint_{\partial BZ_2} \boldsymbol{\partial_k} \chi(\mathbf{k})\, d\mathbf{k} \tag{3.19}$$

which can be seen as the winding number of the gauge transformation on the boundary $\partial BZ_2$. Thus, the Chern number is an obstruction to Stoke's theorem which leads to a quantized Hall conductivity.

## 3.2 Su-Schrieffer-Heeger model (SSH)

The SSH model describes a $1D$ system with a dimerized unit lattice and staggered first-neighbor interactions. Denoting the sublattices by $A$ and $B$, and writing the interactions as $v$ and $w$, the SSH hamiltonian is set to be

$$\hat{H} = v \sum_{m=1}^{N} \left(|m, B\rangle \langle m, A| + h.c\right) + w \sum_{m=1}^{N-1} \left(|m+1, A\rangle \langle m, B| + h.c\right) \tag{3.20}$$

where the first term describes the interaction between elements inside the same cell while the second term represents the intercell interaction. Indexes $m$ are for the $m$-th unit cell. This is a simplified model for polyacetyle, given that a spin-polarized model is being considered here. Writting $|m, A_i\rangle \equiv |m\rangle \otimes |A_i\rangle$ and considering the $2D$ Pauli matrices[16], the hamiltonian can be recast into the following:

$$\hat{H} = v \sum_{m=1}^{N} \left(|m\rangle \langle m| \sigma_x\right) + w \sum_{m=1}^{N-1} \left(|m+1\rangle \langle m| \otimes \frac{\sigma_x + i\sigma_y}{2} + h.c\right) \tag{3.21}$$

In Fourier representation, this last expression can be described by a Tight-Binding (TB) hamiltonian in $k$-space which satisfies

[16] The Pauli matrices are chosen as

$$\sigma_0 = \begin{pmatrix} 1 & 0 \\ 0 & 1 \end{pmatrix} \equiv I; \sigma_x = \begin{pmatrix} 0 & 1 \\ 1 & 0 \end{pmatrix}; \sigma_y = \begin{pmatrix} 0 & -i \\ i & 0 \end{pmatrix} \sigma_z = \begin{pmatrix} 1 & 0 \\ 0 & -1 \end{pmatrix}$$

$$\hat{H}\left|u_n\left(k\right)\right\rangle = E_n\left|u_n\left(k\right)\right\rangle \tag{3.22}$$

with periodic boundary conditions for the bulk states. In the simplest situation, a 2-band model, the hamiltonian reads as follows:

$$\hat{H}\left(k\right) = \begin{pmatrix} 0 & v + we^{-ik} \\ v + we^{ik} & 0 \end{pmatrix} \tag{3.23}$$

On-site energies are set to zero. The dispersion relation is given by

$$E = \sqrt{v^2 + w^2 + 2vwcos\left(k\right)} \tag{3.24}$$

Since any 2-band model bulk hamiltonian can be generically described by

$$\hat{H}\left(k\right) = d_x\left(k\right)\sigma_x + d_y\left(k\right)\sigma_y + d_z\left(k\right)\sigma_z = d_0\left(k\right)\sigma_0 + \mathbf{d}\left(k\right)\cdot\boldsymbol{\sigma} \tag{3.25}$$

one can rewrite the SSH $k$-space hamiltonian in this fashion:

$$\left(v + wcos\left(k\right)\right)\sigma_x + wsin\left(k\right)\sigma_y \tag{3.26}$$

Thus, the components for $\mathbf{d}\left(k\right)$ in the SSH model are $d_0\left(k\right) = d_z\left(k\right) = 0$, $d\left(k\right) = v + wcos\left(k\right)$ and $d_y\left(k\right) = wsin\left(k\right)$. It is important to understand the meaning of $\mathbf{d}\left(k\right)$.Consider $N$ parameters

$$\left\{d_1, d_2, ..., d_{N-1}, d_N\right\}$$

grouped in $\mathbf{d}\left(k\right)$. This is the vector smoothly variated along a path in the parameter space such that

$$\hat{H} = \hat{H}\left(\mathbf{d}\right); \mathbf{d} \in \mathbb{R}^3 \setminus \left\{0\right\} \tag{3.27}$$

It is obvious that $\mathbb{R}^3$ is the parameter space. One can use Bloch's sphere to represent the hamiltonian. By doing so one finds

$$cos\left(\theta\right) = \frac{d_z}{\left|\mathbf{d}\right|}; e^{i\phi} = \frac{d_x + id_y}{\sqrt{d_x^2 + d_y^2}} \tag{3.28}$$

Given that we are working on a 2-band model, the eigenvalues will be $\pm\left|\mathbf{d}\right|$, such that

$$\hat{H}\left|\pm\mathbf{d}\right\rangle = \pm\left|\mathbf{d}\right|\left|\pm\mathbf{d}\right\rangle \tag{3.29}$$

The structure of the eigenstates in momentum space is determined by the direction of $\mathbf{d}$. Due to periodicity ($k = 0 \longrightarrow 2\pi$), joining all the points from different orientations of this vector will give rise to a closed loop in the parameter space. Particularly, it will be a circle of radius $w$ since $d_z = 0$; thus, the vector $\mathbf{d}$ will be contained in $\mathbb{R}^2$. The topological invariant for the SSH model

is the winding number, which defines how many times the trajectory wraps around the origin. This fact is related to a quiral symmetry whose quiral operator must obey

$$\hat{\Gamma}\hat{H}(k)\hat{\Gamma}^{\dagger} = -\hat{H} \tag{3.30}$$

The previous condition is satisfied by $\sigma_z$. Considering a common 2-band hamiltonian and applying the quiral symmetry:

$$\sigma_z\hat{H}(k)\sigma_z^{\dagger} == \begin{pmatrix} d_o + d_z & -d_x + id_y \\ -d_x - id_y & d_o - d_z \end{pmatrix} \tag{3.31}$$

Hence the following relations must be fulfilled:

$$d_o + d_z = -(d_o + d_z) \tag{3.32}$$

$$d_o - d_z = -(d_o - d_z) \tag{3.33}$$

which implies $d_o = d_z = 0$. This result is something already mentioned, but we have proven that the origin for this terms to vanish has a quiral nature. A necessary analysis has to be performed in order to understand the difference between bulk and edge states. Invariance under traslations is a property of the bulk, which allows to consider its states as delocalized. However edge states have a localized character in the thermodynamic limit. Different hopping amplitudes combinations are studied below. Taking $v = 1, w = 0$ one has

$$E = \pm 1 \tag{3.34}$$

where $k$ independence is observed (flat band limit). This parameter combination descibes a model with no interactions between different unit cells. If one thinks about the real edges of the chain, it is clear that no changes respect to the bulk states will arise. If, on the contrary, one chooses $v = 0, w = 1$, although the eigenvalues remain being $E = \pm 1$, a notorious difference shows up. Given that intracell interactions are being neglected while intercell interactions are not, edge atoms will not have a neighbor atom to interact with. This corresponds to, in example,

$$\hat{H}|N, B\rangle = 0; \hat{H}|1, A\rangle = 0 \tag{3.35}$$

Thus, edge states will have zero-energy eigenvalues. The fact that they differ from the bulk states has exceptional consequencies. The election for $v$ y $w$ has a topological implication. Since vector $\mathbf{d}(k)$ depends on the hopping amplitudes, its orientation on every 1BZ point will also depend on them. Consider different combinations for $v$ and $w$:

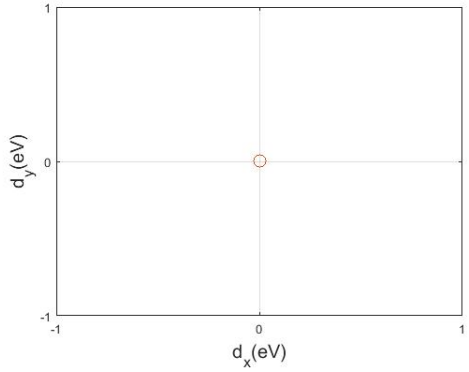


Figura 3: *$d_y$ vs $d_x$ picture for $v = 1$, $w = 0$. This implies that, for these combination, vector $\mathbf{d}(k)$ reduces to a point. No wrapping exists around the origin.*

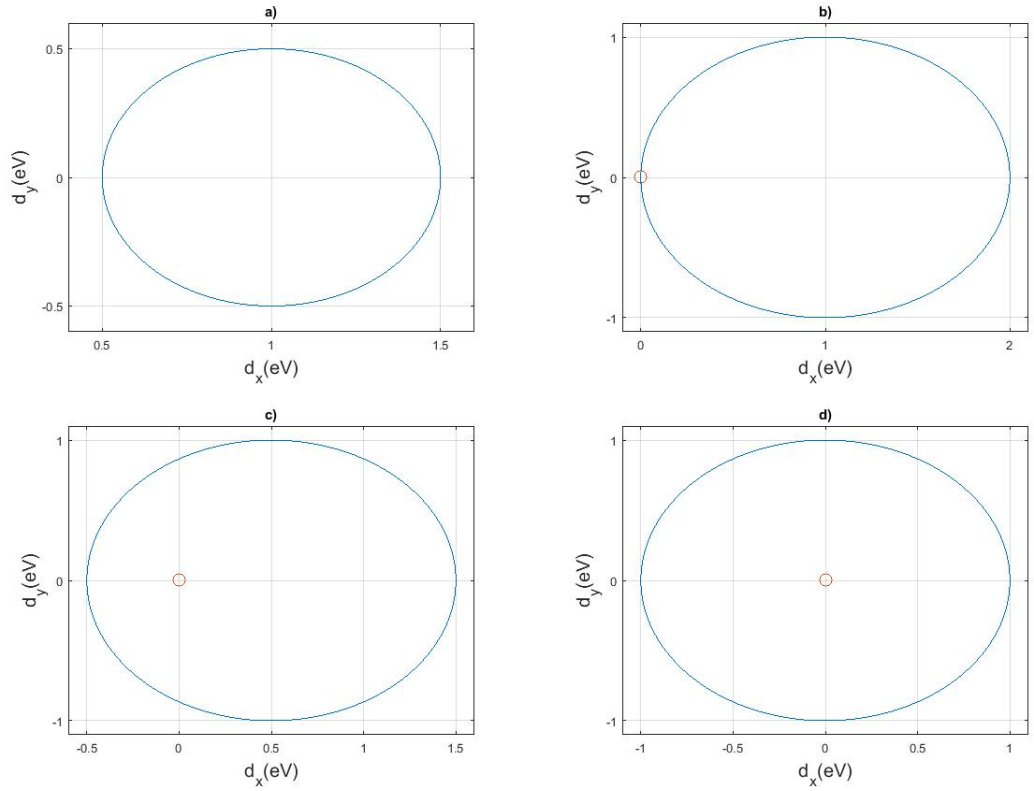


Figura 4: *a) $d_y$ vs $d_x$ picture for $v = 1$, $w = 0{,}5$. As expected, no wrapping happens at the origin. b) $d_y$ vs $d_x$ picture for $v = 1$ and $w = 1$. This is a special situation where the origin is touched an infinite number of times, but not wrapped. c) $d_y$ vs $d_x$ picture for $v = 0{,}5$ and $w = 1$. The winding number is the unit under this conditions. d) $d_y$ vs $d_x$ picture for $v = 0$ and $w = 1$. As in the previous parametrization the winding number is the unit.*

As shown in Figure 4, there is a situation where the winding number is not well-defined, which occurs for $v = w = 1$. This corresponds to a topological phase transition. For $v > w$, the winding number is null, which describes a trivial topological phase. However, for $v < w$, one finds that the winding number is the unit, which is associated to a non-trivial topological phase. This

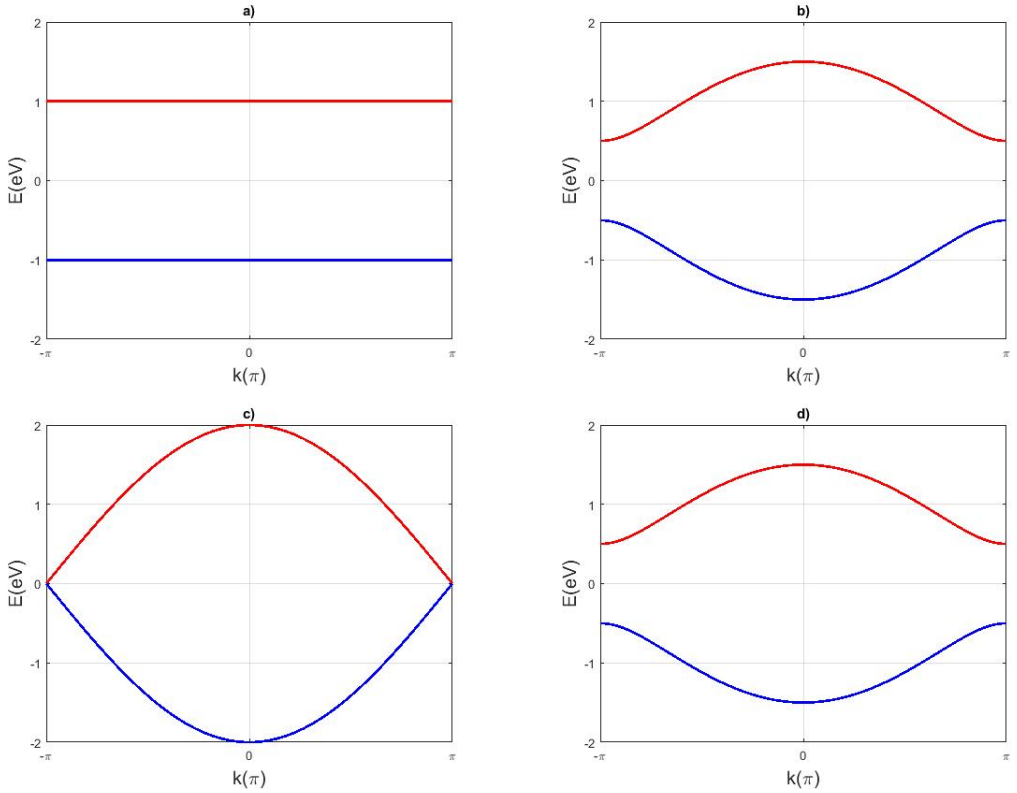


Figura 5: *a) Band structure in the 1BZ for the SSH model with parameters* $v = 1, w = 0$. *b) Band structure in the 1BZ for the SSH model with parameters* $v = 1, w = 0.5$ . *c) Band structure in the 1BZ for the SSH model with parameters* $v = 1$, $w = 1$. *d) Band structure in the 1BZ for the SSH model with parameters* $v = 0{,}5, w = 1$.

topological variation from one situation to another implies that no smooth deformations can be performed on the hamiltonian to change from one phase to the other, which is the basis of a topological phase transition: one cannot deform continuously a system with a given topological invariant into another with a different one; this is, no homotopy can be stablished between the hamiltonians. Hence no adiabatic deformations on the hamiltonian can be performed to change the topological phase. Another contribution to the explanation is the appearance of edge states, which different from those of the bulk.

Figure 5 shows the band structure in the SSH model depends on the hopping amplitudes $v$ and $w$. A topologically trivial phase occurs for Figure 5.a and Figure 5.b while a non-trivial phase happens for Figure 5.d. Figure 5.c shows a transition between topologically trivial and topologically non-trivial phases. As expected, a band gap closure is observed.

When dealing with non-zero eigenvalues, it is known that the eigenstate have a quiral partner on the same lattice, while if the eigenvalue is null, the eigenstates with this same energy belong to different lattices. When an adiabatic variation is performed to the parameter vector $\mathbf{d}$, an edge state can appear, in example,

$$|\psi\rangle \longrightarrow_d |\psi_0\rangle \, , E_0 = 0 \tag{3.36}$$

Due to the quiral symmetry of the system, a modification on the eigenstate also implies a variation over its quiral partner with an eigenvalue that is the zero energy. Because of this, no change in the difference between the number of states $N_A - N_B$ occurs. An inverse consideration can be done. One can start from the edge states with zero energy and perform an adiabatic transformation which creates non-zero energy states. Quirality is responsible for the reduction of the number of states in sublattice A as well as in sublattice B. Thus, $N_A - N_B$ remains constant. Considering that an adiabatic deformation can only occur at the same topological phase, the difference in the number of states $N_A - N_B$ can be viewed as a topological invariant: it remains constant during the whole transformation inside a given phase.

Two topological invariants have been defined in the SSH model. A first one, the winding number, describes the wrapping around the origin in the parameter space. It is also known as the bulk winding number. A second one measuring the difference in the number of states between sublattices has also been introduced. In fact, a bulk topological invariant can be related to the number of edge states. This is the well-known bulk-edge correspondence, a phenomenon which is fundamental in topological condensed matter physics.

## 3.3 Graphene

Since graphene physics is a poweful framework to study theoretical issues such as symmetries and their relation to trivial or non-trivial topological states, different graphene systems are studied below in terms of their symmetries, which are inversion and time reversal.

### 3.3.1 Inversion and time-reversal symmetric model for graphene

A graphene honeycomb lattice is shown below[17]:

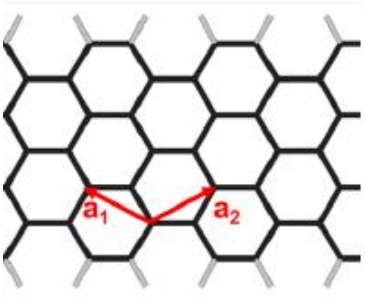


Figura 6: *Honeycomb lattice for graphene and lattice vectors [23].*

The hamiltonian is the following:

[17] Note that the reference system can be chosen such that the $x$ axis goes along the vector $\mathbf{a}_1$ while the $y$ axis is perpendicular to it. Other choices are also plausible.

$$\hat{H} = \sum_i \epsilon \left( \hat{a}_i^\dagger \hat{a}_i + \hat{b}_i^\dagger \hat{b}_i \right) - t \sum_{<i,j>} \left( \hat{a}_i^\dagger \hat{b}_j + \hat{b}_i^\dagger \hat{a}_j \right) \tag{3.37}$$

where $\epsilon$ describes the on-site energy of the electrons and $t$ the first-neighbor hopping amplitude. Thus, the first term describes the electron energy while the second one denotes the hopping energy, where $t$ is the hopping integral between 2 neighbouring lattice positions. The Fourier representation for this hamiltonian is the following:

$$\hat{H} = \sum_k \epsilon \left( \hat{a}_k^\dagger \hat{a}_k + \hat{b}_k^\dagger \hat{b}_k \right) - t \sum_k f(\mathbf{k}) \hat{a}_k^\dagger \hat{b}_k + h.c. \tag{3.38}$$

The Fourier representation of the hamiltonian can be decomposed as

$$\hat{H} = \sum_k \begin{pmatrix} \hat{a}_k^\dagger & \hat{b}_k^\dagger \end{pmatrix} \begin{pmatrix} \epsilon & -tf(\mathbf{k}) \\ -t^* f^*(\mathbf{k}) & \epsilon \end{pmatrix} \begin{pmatrix} \hat{a}_k \\ \hat{b}_k \end{pmatrix} =$$

$$= \sum_k \begin{pmatrix} \hat{a}_k^\dagger & \hat{b}_k^\dagger \end{pmatrix} h(\mathbf{k}) \begin{pmatrix} \hat{a}_k \\ \hat{b}_k \end{pmatrix} \tag{3.39}$$

In order to obtain the dispersion relation, one has to diagonalize $h(\mathbf{k})$, getting this result:

$$\varepsilon(\mathbf{k}) = \epsilon \pm |t| \, |f(\mathbf{k})| \tag{3.40}$$

where the gap energy is defined as $\triangle\varepsilon\,(\mathbf{k}) = 2\,|t|\,|f(\mathbf{k})|$. The factor $f(\mathbf{k})$ is obtained to be

$$f(\mathbf{k}) = 1 + e^{ic\left(-k_x + \frac{k_y}{\sqrt{3}}\right)} + e^{-ic\left(k_x + \frac{k_y}{\sqrt{3}}\right)} \tag{3.41}$$

where $c = \frac{\sqrt{3}a}{2}$ is the lattice constant. Thus, the energy gap can be expressed as

$$\triangle\epsilon\,(\mathbf{k}) = 2 \mid t \mid \sqrt{1 + 4cos\left(\frac{1}{\sqrt{3}} k_y c\right) \left[ cos\left(\frac{1}{\sqrt{3}} k_y c\right) + cos\,(k_x c) \right]} \tag{3.42}$$

A non-zero gap means that our material is an insulator, but there can be some points in the 1BZ where the gap closes. These are the $\pm K$ points, where the two bands get together, also known as Dirac points or Dirac nodes. A Taylor expansion can be performed around the Dirac points as $\mathbf{k} = \pm K + \mathbf{q}$ :

$$f(\pm K + \mathbf{q}) \simeq f(\pm K) + \boldsymbol{\partial}_{\mathbf{k}} f(\mathbf{k}) \mid_{\pm K} .\mathbf{q} \tag{3.43}$$

It is clear that $f(K) = 0$ and $\boldsymbol{\partial}_{\mathbf{k}} f(\mathbf{k}) \mid_{\pm K} \cdot\mathbf{q} = -\sqrt{3}c\,(q_x - iq_y)$. Doing the same around the other point one gets a similar result. Evaluating at a point near the Dirac nodes, the hamiltonian transforms like this:

$$h(\mathbf{k}) \mid_{\mathbf{q}} \backsimeq \begin{pmatrix} \epsilon & \sqrt{3}ct\,(q_x - iq_y) \\ \sqrt{3}ct\,(q_x + iq_y) & \epsilon \end{pmatrix} \tag{3.44}$$

Since we are dealing with a 2-band model, one can always rewrite the hamiltonian in terms of the Pauli matrices:

$$h(\mathbf{k}) \mid_{\mathbf{q}} = \epsilon I + v_f \mathbf{q} \cdot \boldsymbol{\sigma}$$

where $v_f = \sqrt{3}ct$, which is in the order of $10^6 \left(m \cdot s^{-1}\right)$. Avoiding the on-site contribution, we obtain the well-known Dirac equation for massless fermions, also known as the Weyl equation. Electrons behave as massless particles at the Dirac points, this is, as Dirac particles.[18].

There are no other independent Dirac nodes in the problem. The presence of these nodes renders graphene to be a semimetal, with fundamentally different properties from an insulator, because low-energy excitations are always present in such a system. The question one should now ask is whether these Dirac points are stable to perturbations. Our expansion of the Hamiltonian has shown us the existence of two Dirac fermions. However, the Hamiltonian we used was by no means generic. For example, it contained only nearest-neighbor coupling with $C3$ symmetry, and it did not allow for different on-site energies of the A and B sites in the unit cell, etc. Would adding small perturbations to the graphene lattice result in the gapping of these Dirac fermions? What are the perturbations we are allowed to add while keeping the system a semimetal? What kind of perturbations open a gap? For all these questions, we need to look at the symmetries of graphene.

### 3.3.2 Broken inversion symmetry model for graphene

In order to break inversion symmetry, one can do several changes. A simple one[19] is to change the on-site contributions, in example, as follows:

$$\epsilon_A = \epsilon, \epsilon_B = -\epsilon \longrightarrow \sum_k \epsilon \left(\hat{a}_k^\dagger \hat{a}_k - \hat{b}_k^\dagger \hat{b}_k\right) \tag{3.45}$$

It is straightforward to calculate the Fourier representation and the dispersion energy:

$$h\left(\mathbf{k}\right) = \begin{pmatrix} \epsilon & -tf(\mathbf{k}) \\ -t^* f^*(\mathbf{k}) & -\epsilon \end{pmatrix} \tag{3.46}$$

$$\varepsilon(\mathbf{k}) = \epsilon \pm \sqrt{|t|^2 \left|f(\mathbf{k})\right|^2 + \epsilon^2} \tag{3.47}$$

Now the gap obtained is $\varepsilon\left(\mathbf{k}\right) = 2\epsilon$. Since there is no dependence on $\mathbf{k}$, one can conclude that the material will behave as a conventional insulator: there is no way for the bands to close. Performing the same Taylor expansion as the one in the previous section, it is clear that

$$h(\mathbf{k}) \mid_{\mathbf{q}} = \epsilon \begin{pmatrix} 1 & 0 \\ 0 & -1 \end{pmatrix} + t\frac{3a}{2} \begin{pmatrix} 0 & q_x - iq_y \\ q_x + iq_y & 0 \end{pmatrix} = \epsilon\sigma_z + \hbar v_f \mathbf{q} \cdot \boldsymbol{\sigma} \tag{3.48}$$

[18] This model is just a nearest-neighbor approach, but it is enough accurate to show the influence of the symmetries on the system.

[19] Some others such as considering second nearest-neighbor interactions can also break this symmetry.

Eq. (3.48) is the Dirac hamiltonian for electrons with mass, where the mass term is given by $\epsilon\sigma_z$.

### 3.3.3 Haldane's model

Haldane's model describes the behaviour of a graphene model and gives rise to important pedagogical results that can be applied to topological materials such as TI's or TMDC's. In fact, at first sight graphene can be viewed as a TI but its low energy characteristics (in example, its low SOC gap) difficults its application as TI. Haldane's model is a powerful tool to get a first insight into $2D$ topological physics. In addition, it can be also useful since TMDC's are also honeycomb-like materials with 2 sublattices.

Haldane's model [24] breaks temporal inversion symmetry by adding second nearest interactions while applying a perpendicular effective magnetic field such that the net flux through the unit cell is zero. Considering a second-neighbor term like

$$-t' \sum_{<<i,j>>} \left( \hat{a}_i^\dagger \hat{a}_j - \hat{b}_i^\dagger \hat{b}_j \right) \tag{3.49}$$

the second-neighbor interactions are only possible for identical atoms (this is, atoms with the same sublattice index). In addition, a magnetic field implies a phase factor to appear in the hopping integrals, known as Peierls substitution. A magnetic field, and thus, a space-dependent potential vector, breaks the commutation between the hamiltonian and the translation operator, whose consequence is the loose of periodicity and thus the validity of Bloch's theorem. In order to solve this situation, it becomes necessary to use new traslation operators which do commute with the hamiltonian. These are the so-called magnetic traslation operators. They act on a position $\mathbf{R}_i$ destroying an electron on it and creating it at $\mathbf{R}_i + \mathbf{R}_j$ at the expense of adding a path- and magnetic field-dependent phase as

$$\theta_i = \int_{\mathbf{R}_i}^{\mathbf{R}_i+\mathbf{R}_j} \mathbf{A}(x,y) d\mathbf{r} \tag{3.50}$$

Magnetic traslation operators are, then:

$$T_{R_j} = \hat{a}^\dagger_{\mathbf{R}_i+\mathbf{R}_j} \hat{a}_{\mathbf{R}_{ii}} e^{i\theta_i} \tag{3.51}$$

and the new Bloch states will be the following:

$$|\psi_\mathbf{k}\rangle = \frac{1}{N} \sum_\mathbf{R} e^{i(\mathbf{kR} + \frac{q}{\hbar}\theta)} |\psi_\mathbf{R}\rangle \tag{3.52}$$

Appendix B.2 proves the following results. The final hamiltonian is this:

$$\hat{H} = \sum_i \epsilon \left( \hat{a}_i^\dagger \hat{a}_i - \hat{b}_i^\dagger \hat{b}_i \right) - t \sum_{<i,j>} \left( \hat{a}_i^\dagger \hat{b}_j + \hat{b}_i^\dagger \hat{a}_j \right) - t' \sum_{<<i,j>>} e^{i\frac{q}{\hbar}\theta_{ij}} \left( \hat{a}_i^\dagger \hat{a}_j - \hat{b}_i^\dagger \hat{b}_j \right) \tag{3.53}$$

which, in Fourier representation looks like follows :

$$\hat{H} = \sum_k \begin{pmatrix} \hat{a}_k^\dagger & \hat{b}_k^\dagger \end{pmatrix} \begin{pmatrix} \epsilon & -tf(\mathbf{k}) \\ -t^* f^*(\mathbf{k}) & -\epsilon \end{pmatrix} \begin{pmatrix} \hat{a}_k \\ \hat{b}_k \end{pmatrix} -$$

$$-t' \sum_k \begin{pmatrix} \hat{a}_k^\dagger & \hat{b}_k^\dagger \end{pmatrix} \begin{pmatrix} f(\mathbf{k})t' e^{i\frac{q}{\hbar}\theta_{ij}} + h.c. & 0 \\ 0 & f^*(\mathbf{k})t' e^{i\frac{q}{\hbar}\theta_{ij}} + h.c. \end{pmatrix} \begin{pmatrix} \hat{a}_k \\ \hat{b}_k \end{pmatrix} \tag{3.54}$$

with

$$h_0(\mathbf{k}) = \begin{pmatrix} \epsilon & -tf(\mathbf{k}) \\ -t^* f^*(\mathbf{k}) & -\epsilon \end{pmatrix} \tag{3.55}$$

$$h_1(\mathbf{k}) = \begin{pmatrix} f(\mathbf{k})t' e^{i\frac{q}{\hbar}\theta_{ij}} + h.c. & 0 \\ 0 & f^*(\mathbf{k})t' e^{i\frac{q}{\hbar}\theta_{ij}} + h.c. \end{pmatrix} \tag{3.56}$$

Diagonal terms for $h_1(\mathbf{k})$ are worked in Appendix B.3. One finds the whole hamiltonian $h(\mathbf{k})$ can be rewritten as a 2-band hamiltonian like $\hat{H} = \begin{pmatrix} d_o + d_z & d_x - id_y \\ d_x + id_y & d_o - d_z \end{pmatrix}$. The diagonal terms are:

$$\begin{aligned} d_o &= -2t' cos\left(\tfrac{q}{\hbar}\theta_{ij}\right)\left(cos\left(\mathbf{k}\boldsymbol{\delta}_1\right) + \left(\mathbf{k}\boldsymbol{\delta}_2\right) + \left(\mathbf{k}\boldsymbol{\delta}_3\right)\right) \\ d_z &= \varepsilon + 2t' sin\left(\tfrac{q}{\hbar}\theta_{ij}\right)\left(sin\left(\mathbf{k}\boldsymbol{\delta}_1\right) + \left(\mathbf{k}\boldsymbol{\delta}_2\right) + \left(\mathbf{k}\boldsymbol{\delta}_3\right)\right) \end{aligned} \tag{3.57}$$

while the off-diagonal ones are:

$$\begin{aligned} d_x &= tRe\left(f(\mathbf{k})\right) = t\left(cos\left(\mathbf{k}\mathbf{a}_1\right) + cos\left(\mathbf{k}\mathbf{a}_2\right) + cos\left(\mathbf{k}\mathbf{a}_3\right)\right) \\ d_y &= tIm\left(f(\mathbf{k})\right) = t\left(sin\left(\mathbf{k}\mathbf{a}_1\right) + sin\left(\mathbf{k}\mathbf{a}_2\right) + sin\left(\mathbf{k}\mathbf{a}_3\right)\right) \end{aligned} \tag{3.58}$$

By solving the characteristic equation the following dispersion relation is found

$$\epsilon = d_o \pm |d(\mathbf{k})| \tag{3.59}$$

Appendix B.4 shows the calculation of the valence band eigenstate:

$$|\psi_-\rangle = \frac{1}{2d(\mathbf{k})\left[d(\mathbf{k}) - d_z\right]} \begin{pmatrix} d_z - |d(\mathbf{k})| \\ d_x + id_y \end{pmatrix} \tag{3.60}$$

It is important to note that, as for the generic case, there is a singular situation if $d_x = d_y = 0, d_z > 0$. A gauge transformation which conserves the probability amplitude has to be performed in order to avoid this problem:

$$\left|\psi_-'\right\rangle = \frac{1}{N'} \begin{pmatrix} -d_x + id_y \\ d_z + |d(\mathbf{k})| \end{pmatrix} \tag{3.61}$$

But now the same problem arises for $d_x = d_y = 0, d_z < 0$. This has to do with the topology of the parameter space. The election of one or another wavefunction will depend on the region (as the problem of the magnetic monopole). Specifically, the points where these situations happen

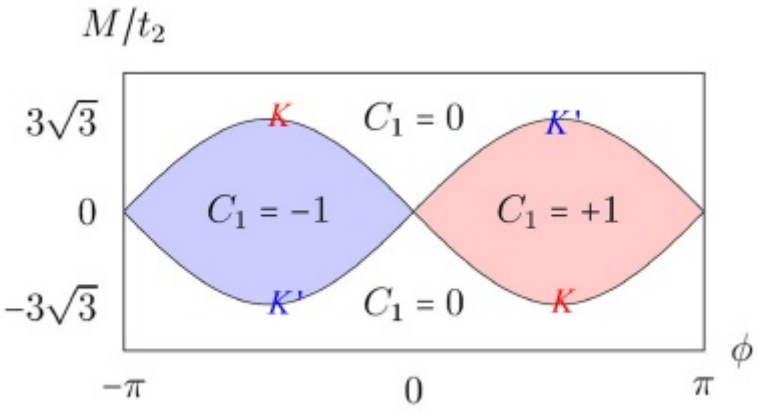


Figura 7: *Picture describing the topological order by the Chern number in terms of the mass and the phase [25]. In this picture, M denotes what we have named $\epsilon$ , while K y K′ are the symmetry points (denoted by $\pm K$ in this work).*

are $\pm K$. Evaluating the hamiltonian at these points one gets

$$d_x = d_y = 0 \tag{3.62}$$

$$d_z\left(K\right) = 3\sqrt{3}t' sin\phi + \epsilon \tag{3.63}$$

$$d_z\left(-K\right) = -3\sqrt{3}t' sin\phi + \epsilon \tag{3.64}$$

where $\phi$ is the gauge phase from the gauge transformation made in eq. (3.61). As well as in the QHE, a topological invariant, the Chern number, can be defined and studied for Haldane's model. Working with just one band (on the contrary, the topological invariant would be the sum of every Chern number) and considering $sin\phi > 0$, one gets the following Chern number :

$$C = 1 \tag{3.65}$$

while if $sin\phi < 0$ had been considered, the result would have been

$$C = -1 \tag{3.66}$$

Chern's number is the topological invariant of the system. Figure 7 depicts the relation between different topological phases and the mass and phase parameters $\epsilon$ and $\phi$ (note that the $d_z$ term is the one that will determine the topological nature of the system) in the Chern number for the Haldane's model. Given that two values are possible, a third transition value $C = 0$ can be also possible.

Regions with Chern number $C_1 = 0$ are those associated with a conventional insulator. Those

ones in which the Chern number is non-zero ($C_1 = \pm 1$) are related to a topological insulator, known as Chern insulator in this context. In the limit case

$$|\epsilon| = 3\sqrt{3}\left|t' sin\phi\right| \tag{3.67}$$

the gap is broken and thus the bands close. This is the situation for which a singularity in the wavefunction occurs ($d_x = d_y = d_z = 0$) at $K$ and $-K$.

We may be interested in the edge states and the way the hamiltonian behaves at those points. As done before at $K$, but now considering the $d_o$ and $d_z$ components (notice that the behaviour of $h_o(\mathbf{k})$ is already known):

$$d_o(K+\mathbf{q}) \pm d_z(K+\mathbf{q}) \simeq d_o(K) \pm d_z(K) + \boldsymbol{\partial}_{\mathbf{k}} d_o(\mathbf{k}) \mid_K .\mathbf{q} \pm \boldsymbol{\partial}_{\mathbf{k}} d_z(\mathbf{k}) \mid_K .\mathbf{q} \tag{3.68}$$

Finally, after calcuting $\boldsymbol{\partial}_{\mathbf{k}} d_o(\mathbf{k}) \mid_K$ and $\boldsymbol{\partial}_{\mathbf{k}} d_z(\mathbf{k}) \mid_K$ the result is found to be

$$d_o(K+\mathbf{q}) + d_z(K+\mathbf{q}) \simeq d_o(K) \pm d_z(K) \tag{3.69}$$

and thus

$$h_1(\mathbf{k}) \simeq \begin{pmatrix} d_o(K) + d_z(K) & 0 \\ 0 & d_o(K) - d_z(K) \end{pmatrix} \tag{3.70}$$

for points near $K$. A final expression for the Dirac hamiltonian can be written as follows:

$$\hat{H} = d_o(K) I + \hbar v_f \mathbf{q} \cdot \boldsymbol{\sigma} + d_z(K)\sigma_z \tag{3.71}$$

where $d_z(K)$ is a term that can be implemented as, in example, a magnetization.

## 3.4 Quantum Spin Hall Effect (QSHE). Topological Insulators (TI's)

The QSHE phase is introduced in the following section, considering the Kane-Mele model [15,16] for graphene with SOC. It is remarkable that the SOC in graphene is so small that it cannot provide (by now) a suitable experimental implementation, but this is a cornerstone model in order to study topological insulators and topological phases in general.

Although a lot of work has be performed, TI's have still not been introduced. In order to have a TI, a SOC has to appear (and be strong enough). The QHSE can be viewed as a duplication of the QHE with opposite conductances. Materials with QSHE have TRS since $\hat{J}_x^s = \hat{\sigma}_{xy}^s \hat{E}_x$ is even under $\hat{T}$. A common TI has a band structure with a gap in the bulk between the valence band and the conduction band. However, there will be edge states (as in QHE) with a non-zero conductivity. Since the QSHE is a doubled version of the QHE, two Hall conductivities will appear depending on the spin. As one can figure out, this will lead to the appearance of two

opposite Chern numbers. If one is looking for a topological invariant, then the Chern number cannot be a good number. However, a spin Chern number can be defined such that its difference describes the current on the edges.

Based on Haldane's work [24], Kane y Mele [15] proposed a first version for the QHSE based on a model for graphene with SOC and without second-neighbours interactions. The SOC term is the following:

$$\hat{H}_{SOC} = \lambda_{SO} \sum_{i,j,\sigma} i\sigma v_{ij} \left( \hat{c}^{\dagger}_{i\sigma} \hat{c}_{j\sigma} + \hat{b}^{\dagger}_{i\sigma} \hat{b}_{j\sigma} \right) \tag{3.72}$$

where $\hat{c}^{\dagger}_{i\sigma}, \hat{b}^{\dagger}_{i\sigma}$ are the creation operators for every sublattice, respectively, and $i, j$ denote unit cells . The factor $v_{ij}$ is $\pm 1$ depending on symmetric ($i$ to $j$) or antisymmetric ($j$ to $i$) transitions:

$$\hat{H}_{SOC} = \lambda_{SO} \sum_{i,j,\sigma} i\sigma v_{ij} \left( \hat{c}^{\dagger}_{i\sigma} \hat{c}_{j\sigma} + \hat{b}^{\dagger}_{i\sigma} \hat{b}_{j\sigma} \right) =$$

$$= -\lambda_{SO} \sum_{i,\sigma} i\sigma \hat{c}^{\dagger}_{i\sigma} \left( \hat{c}_{i+a_1,\sigma} - \hat{c}_{i+a_2,\sigma} + \hat{c}_{i-a_1+a_2,\sigma} - \hat{c}_{i-a_1,\sigma} + \hat{c}_{i-a_2,\sigma} - \hat{c}_{i+a_1-a_2,\sigma} \right) -$$

$$-\lambda_{SO} \sum_{i,\sigma} i\sigma \hat{b}^{\dagger}_{i\sigma} \left( \hat{b}_{i+a_1,\sigma} - \hat{b}_{i+a_2,\sigma} + \hat{b}_{i-a_1+a_2,\sigma} - \hat{b}_{i-a_1,\sigma} + \hat{b}_{i-a_2,\sigma} - \hat{b}_{i+a_1-a_2,\sigma} \right) \tag{3.73}$$

Performing a Fourier transformation as in the previous sections one finds:

$$H_{SOC} = -\lambda_{SO} \sum_{\mathbf{k},\sigma} i\sigma \left( \hat{c}^{\dagger}_{\mathbf{k}\sigma} \hat{c}_{\mathbf{k}\sigma} - \hat{b}^{\dagger}_{\mathbf{k}\sigma} \hat{b}_{\mathbf{k}\sigma} \right) \cdot$$

$$\cdot \left( e^{-i\mathbf{k}\mathbf{a}_1} - e^{-i\mathbf{k}\mathbf{a}_2} + e^{-i\mathbf{k}(\mathbf{a_2}-\mathbf{a}_1)} - e^{i\mathbf{k}\mathbf{a}_1} + e^{i\mathbf{k}\mathbf{a}_2} - e^{i\mathbf{k}(\mathbf{a_2}-\mathbf{a}_1)} \right) =$$

$$= -\lambda_{SO} \sum_{\mathbf{k},\sigma} i\sigma \left( \hat{c}^{\dagger}_{\mathbf{k}\sigma} \hat{c}_{\mathbf{k}\sigma} - \hat{b}^{\dagger}_{\mathbf{k}\sigma} \hat{b}_{\mathbf{k}\sigma} \right) \cdot$$

$$\cdot F \left( e^{-i\mathbf{k}\mathbf{a}_1} - e^{i\mathbf{k}\mathbf{a}_1} - e^{-i\mathbf{k}\mathbf{a}_2} + e^{i\mathbf{k}\mathbf{a}_2} - e^{i\mathbf{k}(\mathbf{a_2}-\mathbf{a}_1)} + e^{-i\mathbf{k}(\mathbf{a_2}-\mathbf{a}_1)} \right) =$$

$$= 2\lambda_{SO} \sum_{\mathbf{k},\sigma} \sigma \left( \hat{c}^{\dagger}_{\mathbf{k}\sigma} \hat{c}_{\mathbf{k}\sigma} - \hat{b}^{\dagger}_{\mathbf{k}\sigma} \hat{b}_{\mathbf{k}\sigma} \right) \left[ sin(\mathbf{k}\mathbf{a}_1) - sin(\mathbf{k}\mathbf{a}_2) - sin(\mathbf{k}(\mathbf{a_1}-\mathbf{a}_2)) \right] \tag{3.74}$$

Defining $C = sin(\mathbf{k}\mathbf{a}_1) - sin(\mathbf{k}\mathbf{a}_2) - sin(\mathbf{k}(\mathbf{a_1}-\mathbf{a}_2))$ and expanding on $\sigma$ one finds

$$h\left(\mathbf{k}\right) = \begin{pmatrix} 2\lambda_{SO}C & 0 & 0 & 0 \\ 0 & -2\lambda_{SO}C & 0 & 0 \\ 0 & 0 & -2\lambda_{SO}C & 0 \\ 0 & 0 & 0 & 2\lambda_{SO}C \end{pmatrix} \tag{3.75}$$

The hamiltonian of the QSHE is a box hamiltonian. Adding the SOC term to the rest of the hamiltonian, which implies to double the latter, one gets

$$\hat{H} = \begin{pmatrix} d_o + d_z + 2\lambda_{SO}C & d_x - id_y & 0 & 0 \\ d_x + id_y & d_o - d_z - 2\lambda_{SO}C & 0 & 0 \\ 0 & 0 & d_o + d_z - 2\lambda_{SO}C & d_x - id_y \\ 0 & 0 & d_x + id_y & d_o - d_z + 2\lambda_{SO}C \end{pmatrix} \tag{3.76}$$

Working at the edge points of the 1BZ it is shown that a mass term appears as $\pm 2\lambda_{SO}C\sigma_z$ for spin up and down respectively.

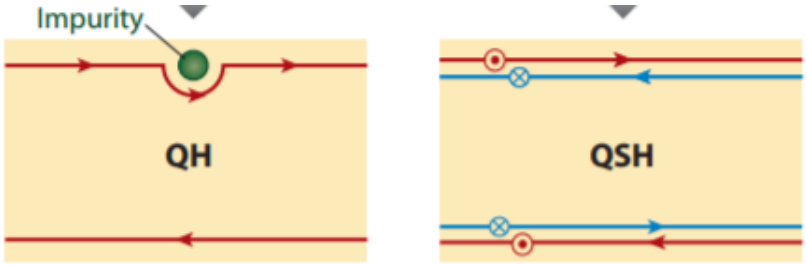


Figura 8: *Schematic comparison between QHE and QSHE [26]. Since QSHE is made of two copies of the QHE, the edge states are also duplicated, and have different quiralities.*

There are two helical modes on each edge. No scattering is allowed as in QHE, since in order to be reflected, the electron has to flip its spin (this is the only fashion to change the propagation direction), and TRS has to be broken in order to do so. Impurities have to be non-magnetic in order to make this change, because if not, TRS would be broken. Spatial separation of the edge states is now produced by SOC, and no external magnetic field is needed (in fact, magnetic field would break TRS). Edge states have opposite group velocities, constituting a topologically protected quiral edge states. As well, each band has a Chern number $C_{\uparrow(\downarrow)} = 1(-1)$, and thus the total Chern number will be zero. QHSE has strong edge states and a gap in the bulk, so it is a topological phase of matter. But in order to characterize its topology, a different topological invariant is needed; the spin Chern number.

$2D$ TI's were predicted by Kane and Mele in 2005 [15]. Their idea was that graphene could behave as a TI through QSHE, which is a reason for naming the TI's as QSHE insulators. Since the energy gap in graphene is quite small, it is not a good candidate. But a different material, the quantum well system made of $HgCdTe$ was shown to behave as a good TI. After this discovery, a big effort has been made and also $3D$ TI's have been implemented [27], but since $3D$ materials are out of the scope of this work, they will not be explained here.

# 4 2D TRANSITION METAL DICHACOGENIDES (TMDC's)

Transition Metal Dichalcogenides (TMDC's) are materials constituted by a transition metal $M$ and a chalcogen $X$ as $MX_2$. Although other point symmetries can occur, those TMDC's with $D_{6h}$ point group symmetry are made of weakly interacting stacked layers of $2D$ $MX_2$ which are often named as $2H$-type $MX_2$, where $2H$ denotes trigonal prismatic symmetry.

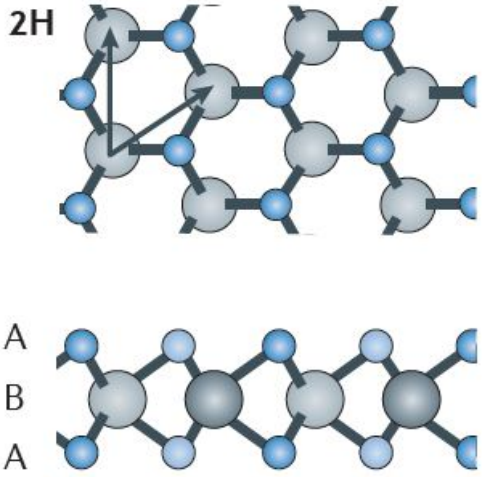


Figure 9: *$2H$-type structure [28]. This is the $2D$ TMDC model this research has dealed with. The top picture shows the lattice vectors between metal atoms, which are denoted by grayish spheres. The blue and smallest spheres depict the chalcogen atoms.*

The bottom picture in Figure 9 shows that chalcogens occupy a position $A$ and are located in the top of each other in a direction that is normal to the layer. The metal atoms at $B$ are between them, and are located at the geometrical center of a trigonal prismatic lattice in which chalcogens are at its vertices positions. The most popular TMDC's are those made of group $VI$ transition metals (mainly $Mo$ and $W$) in combination with chalcogens $S$, $Se$ or $Te$. Since these kind of $2D$ TMDC's are semiconductors in the termodynamically stable $2H$ phase, they are regarded as good candidates for electronic devices. $2D$ TMDC's have a direct gap at $\pm K$ high symmetry points (which are corners of the 1BZ) while bilayer or bulk structures do not. A consequence is that since these are inequivalent high-symmetry points, valley-dependent features can arise. They also lack of inversion symmetry, which causes SOC to split the bands. In addition, the inversion symmetry breaking is responsible for a valley-dependent optical transition selection rule, according to which transitions between the valence and the conduction band (interband transitions) couple to left- (at $K$) or right- (at $-K$) circularly polarized light.

A work on the band structure of monolayer TMDC's and its topological characterization has been performed. The central interest in monolayer TMDC's is related to the direct gap existing at the $\pm K$ points in the 1BZ. While bulk TMDC's do have an indirect gap, monolayer TMDC's have a direct gap that is responsible for the valleytronics. The work that has been developed

on TMDC's lies in the implementation of a module of programs that allow to study the band structure of several 2D TMDC's[20] In order to do so, a particular model has been considered, based in [18]. This model is a 3-band TB model with $d_{z^2}$, $d_{xy}$ and $d_{x^2-y^2}$ orbitals which belong to the metal in the TMDC[21]. $\mathbb{Z}_2$ invariant computation, a major role in this research, has been performed from the band structure information. In addition, a calculation of the Berry curvature and the circular degree of polarization has been obtained.

## 4.1 TB model with $M - d_{z^2}$, $d_{xy}$ and $d_{x^2-y^2}$ orbitals

Although the unit cell of a $MX_2$ TMDC is $3D$, one can consider a $2D$ hexagonal lattice as a first approximation, which is accurate enough to describe the monolayer properties in the low-energy regime. There are 3 types of high symmetry points, depicted below:

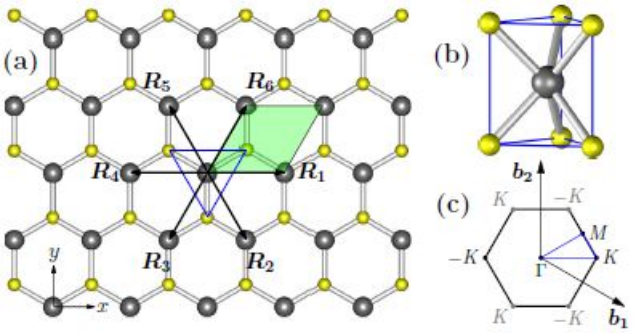


Figure 10: *2D $MX_2$ structure for TMDC's [18]. a) Top view of a $MX_2$ layer. The green-coloured region is the 2D unit cell. Dark spheres represent the metal $M$ while yellow ones depict the chalcogen $X$. Vectors $\{R_i\}$ describe the position of the 6 nearest-neighbor atoms. The chalcogen nearest-neighbor vectors are not considered in this model. b) A 3D view of the trigonal prismatic lattice. c) 1BZ and high symmetry points $\Gamma$, $\pm K$ and $M$.*

The points depicted in Figure 10.c play a major role in the symmetry properties of the TMDC's and in the calculation of the $\mathbb{Z}_2$ invariant. In order to study the band structure, the path $M \longrightarrow -K \longrightarrow \Gamma \longrightarrow K \longrightarrow M$ is depicted. In adition, in order to calculate the $\mathbb{Z}_2$ invariant, a rectangular trajectory involving $\Gamma$ and $M$ points is used.

Due to the $D_{3h}$ point-group symmetry of the trigonal lattice, $2H$-type TMDC's are studied here (Figure 10.a is a good picture of this kind of structures). This symmetry also conditions the following classification of the orbitals in terms of the Mulliken notation for the irreducible representations of the $D_{3h}$ point-group:

[20] Although the research has been focused on $MoS_2$, the band structure of the following TMDC's has also been computed: $MoSe_2$, $MoTe_2$, $WS_2$, $WSe_2$ and $WTe_2$.

[21] A work on a 6-band TB model with $d_{z^2}$, $d_{xy}$ , $d_{x^2-y^2}$ orbitals from $M$ and $p_x$, $p_y$ , $p_z$ orbtitals from $X$ has been pursued. Different approaches have been published, such as those in [29,30], in which the whole orbitals of the highest levels of the 3 atoms of a 3D unit cell are considered. However, the 6-band calculations have been conditioned by the unavailable ab-initio information related to the hopping amplitudes between $p$ and $d$ orbitals found in the references.

$$A_1' \{d_{z^2}\}; E' \{d_{xy}, d_{x^2-y^2}\}; E'' \{d_{xz}, d_{yz}\}$$

Since trigonal prismatic cells have a reflection symmetry by the $XY$ plane, only hybridization between orbitals in $A_1'$ and $E'$ is allowed, which implies that orbitals in $E''$ are decoupled from the other groups and then these can be despised. This justifies the use of a 3-band approximation based on the $d_{z^2}$, $d_{xy}$ and $d_{x^2-y^2}$ orbitals[22].

### 4.1.1 First-neighbor hoppings 3-band TB model for TMDC's

As a first approach, a model with only nearest-neighbor interactions is calculated for different TMDC's. A TB model with $d_{z^2}$, $d_{xy}$ and $d_{x^2-y^2}$ orbitals from the metal $M$ is used, taking into account the influence of the $p$ orbitals in the chalcogen $X$. A numerical simulation is performed in order to obtain the band dispersion for different $MX_2$ TMDC's. Although the results found are not accurate in the whole 1BZ in comparison to the GGA calculations from [18], its accuracy at the $\pm K$ is enough to find some remarkable results. Since TMDC's are considered to be free from impurities, they are considered to be intrinsic semiconductors. The Fermi level is set to zero energy, so the bands are plotted taking into account their distance to the Fermi energy.

Figure 11 shows that a direct gap between the valence and the conduction band is found at $\pm K$ in $MoS_2$, which is qualitatively accurate with the GGA calculations. However, away from this points the results are not as accurate as in the GGA aproximation. This is a reflection of the nearest-neighbor approach. In $MoSe_2$ no direct gap is found in this material at the $\pm K$ points, which is due to the approach considerer in this section. This indirect gap is due to a spurious eigenvalues of the conduction band, which show different behavior than expected. A bigger problem happens for $MoTe_2$, since the valence band has a soft maximun at $\pm K$ while there is no direct gap due to the behavior of the conduction band.

On the contrary, $WS_2$ has well-defined valleys through a direct gap at $\pm K$, as in $MoS_2$. For $WSe_2$, a direct gap at $\pm K$ points is observed, while in $WTe_2$ the result is not accurate with the predictions since the conduction band does not have a minimum at $\pm K$.

It is shown that $MoS_2$ and $WS_2$ have a well-defined direct gap at the $\pm K$ points, which causes the appearance of a valley at each. However, even at these points, results for the rest of TMDC's are not accurate at this points, which is a consecuence of the first-neighbor approximation. Generally, far from the $\pm K$ points every figure indicates that a better accurate model has to be introduced in order to obtain a good behavior, at least at $\Gamma$ and $\pm K$.

[22] This is partially true, since the ab-initio amplitudes and hamiltonian elements have also implicit the contribution of the $p$ orbitals in the chalcogen. However, a good agreement with GDA and LDA information occurs.

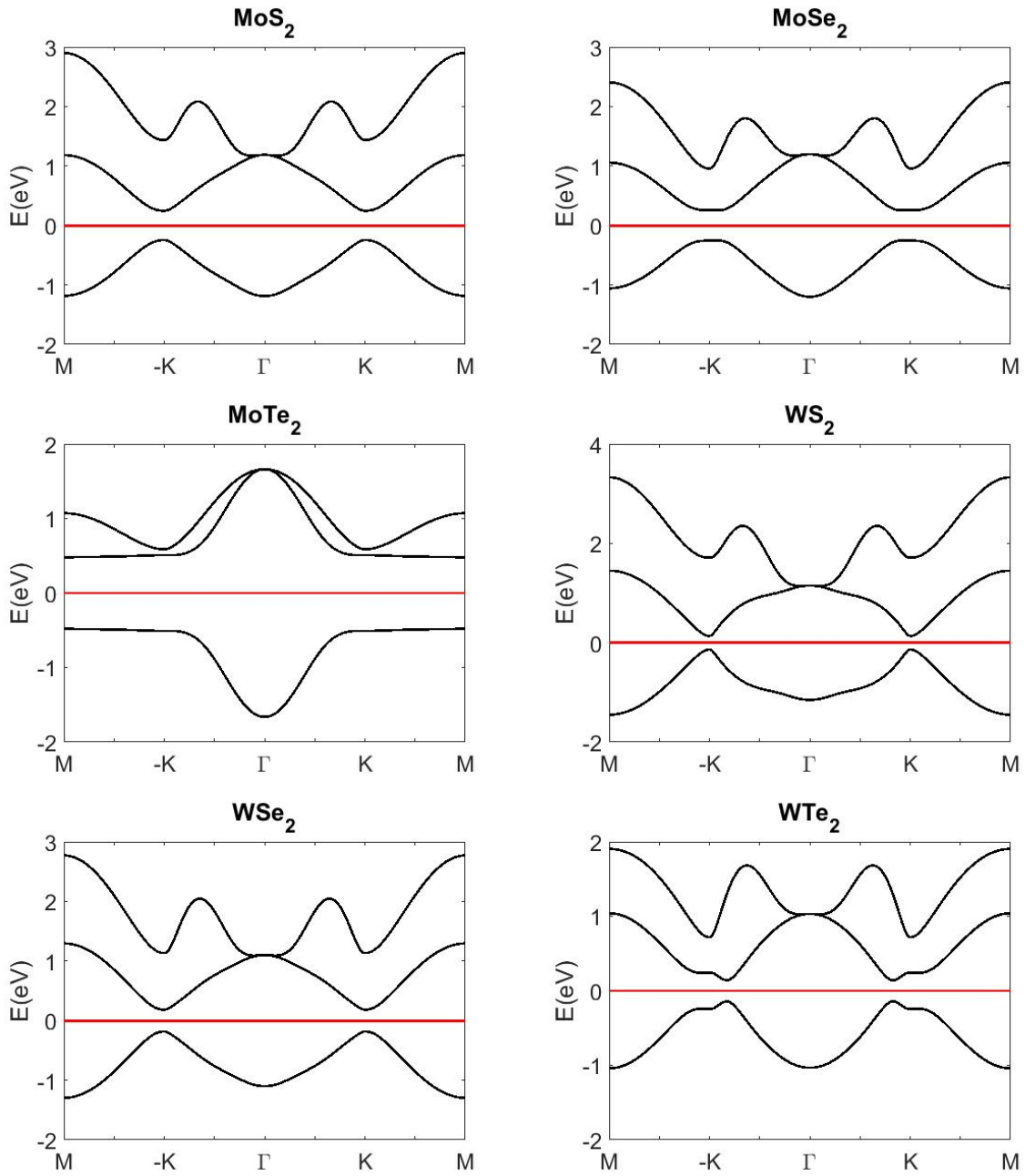


Figure 11: *Band structure in the 3-band model with nearest-neighbor hoppings for different TMDC's across the path* $M \longrightarrow -K \longrightarrow \Gamma \longrightarrow K \longrightarrow M$. *Fermi energy is set to zero.*

### 4.1.2 Up to third-neighbor hoppings 3-band TB model for TMDC's

Since there is not a good fit between the TB band structure and the GGA band structure at other 1BZ points but the ones near $\pm K$, an up to third-neighbor hoppings 3-band TB model is computed. Results for different TMDC's are shown in Figure 12. A good fit is found at $\pm K$ and $\Gamma$ in $MoS_2$, which shows the improvement of the calculations. It must be pointed out that other $\mathbf{k}$ points are not accurate, which is a consequence of the $p$ orbitals strength at these regions. It is also shown that a direct gap is found at $\pm K$ for $MoSe_2$, which is a consequence of the up to third-nearest-neighbor approach. A similar improvement is also observed in $MoTe_2$. For $WS_2$ the gap between the valence and conduction band is extended in comparison with the nearest-neighbor approach, which is a good symptom and a consequence of this new model; in fact, this is observed in all the TMDC's. In the case of $WSe_2$ and $WTe_2$ a direct gap is also stablished.

These approach has improved the behaviour at $\pm K$ and valleys have been accurately defined. In addition, a better approach to the GGA information at $\Gamma$ is found when compared to the nearest-neighbor model. A final comparative table is shown in Figure 13, in which results from the nearest-neighbor and the up to third-neighbor models are compared with the GGA results from [18] for $MoS_2$. The accuracy is enough to perform calculations such as the Berry curvature or the degree of circular polarization, but before going on, let us study SOC in $2H$-type $2D$ TMDC's.

### 4.1.3 Up to third-neighbor hoppings 3-band TB model with SOC for TMDC's

In order to study the SOC effect in the previous model, an up to third-neighbor hoppings 3-band TB model with SOC is implemented. Since the metal atom in $MX_2$ is sufficiently heavier than the chalcogen, only on-site contributions from the $M$ atom are used to introduce the SOC. As any SOC TB model, the matrix dimensions double, since the basis orbitals are now

$$\left\{\left|d_{z^2}\uparrow\right\rangle, \left|d_{xy}\uparrow\right\rangle, \left|d_{x^2-y^2}\uparrow\right\rangle, \left|d_{z^2}\downarrow\right\rangle, \left|d_{z^2}\downarrow\right\rangle, \left|d_{z^2}\downarrow\right\rangle\right\}$$

Taking only the $z$-direction, the usual term $\mathbf{L}\cdot\mathbf{S}$ from the SOC reduces to

$$\mathbf{L}\cdot\mathbf{S} = L_z S_z = \frac{1}{2}\begin{pmatrix} L_z & 0 \\ 0 & -L_z \end{pmatrix} \tag{4.1}$$

This makes our new TB hamiltonian to be

$$H_{SOC} = \begin{pmatrix} H + \frac{\lambda}{2}L_z & 0 \\ 0 & H - \frac{\lambda}{2}L_z \end{pmatrix} \tag{4.2}$$

where $H$ is a $3\times 3$ hamiltonian. A comparison between the nearest-neighbor and the up to third-nearest-neighbor models with SOC in $MoS_2$ is shown:

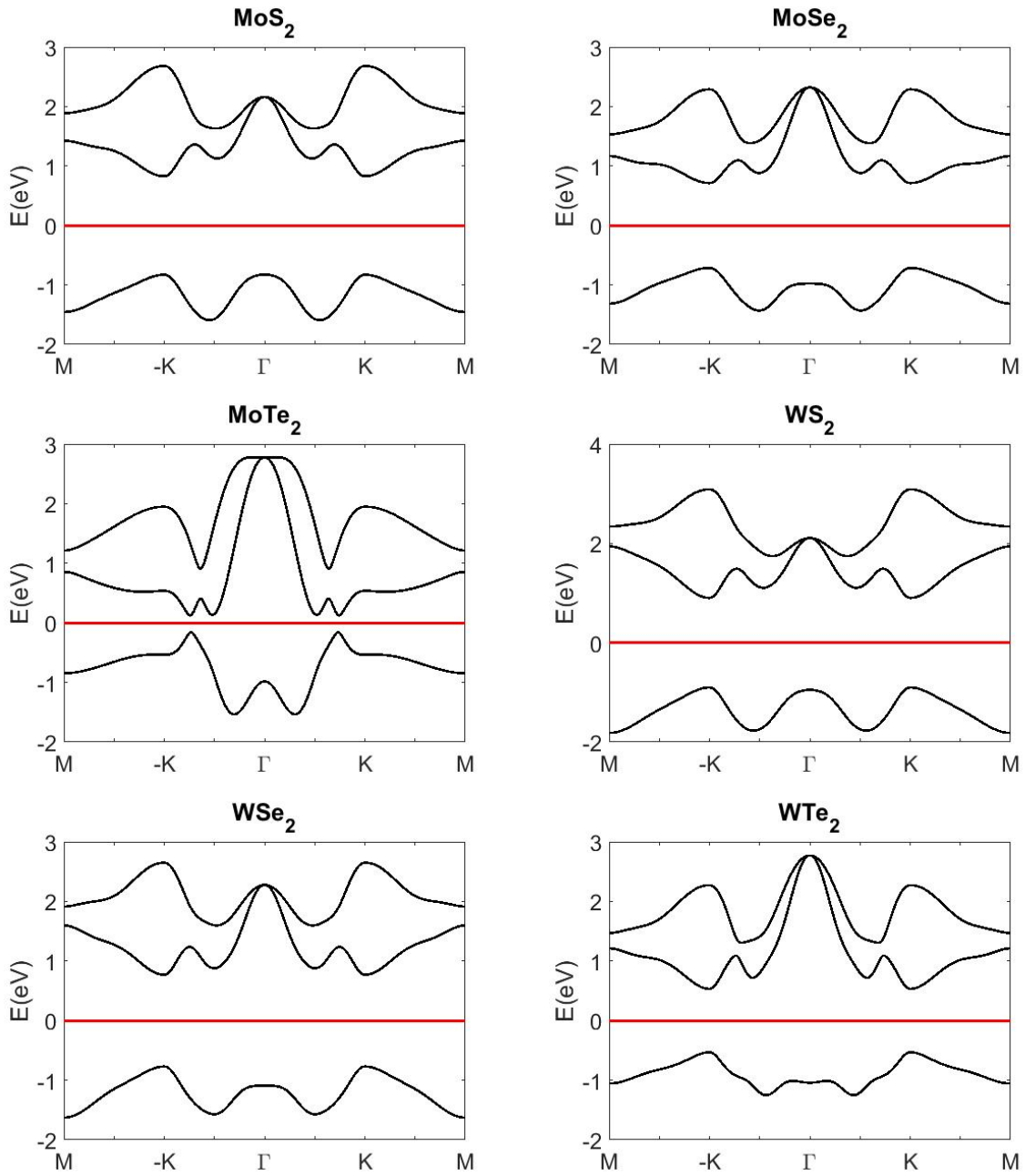


Figure 12: *Band structure for the 3-band model with up to third-neighbor hoppings in different TMDC's across the path* $M \longrightarrow -K \longrightarrow \Gamma \longrightarrow K \longrightarrow M$. *Fermi energy is set to zero.*

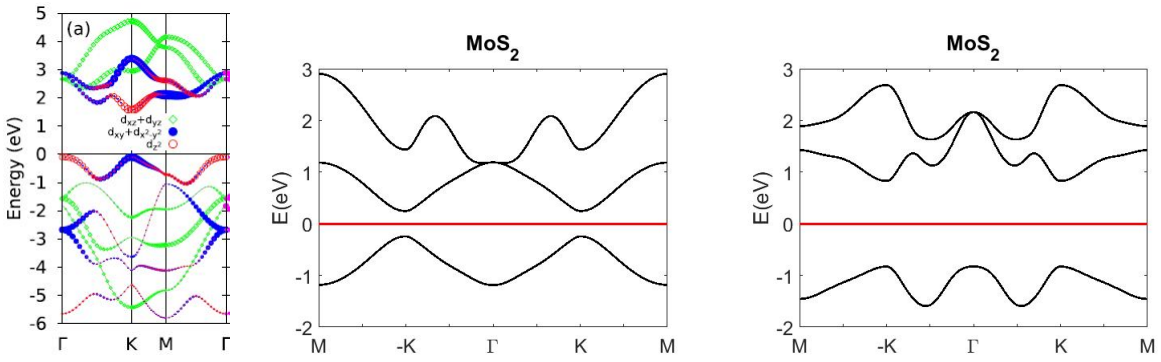


Figure 13: *Comparison between the GGA calculations from [18] (left) and the results for the nearest-neighbor (top right) and the up to third-neighbor (bottom right) models.*

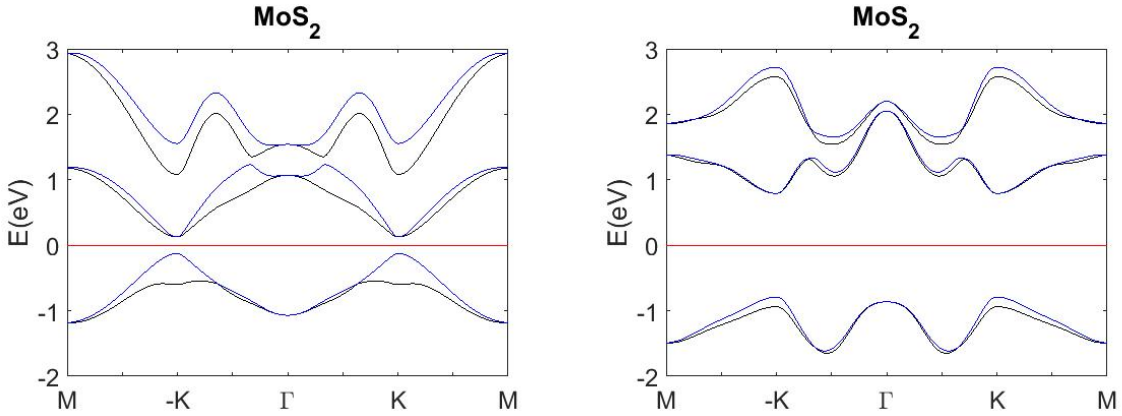


Figure 14: *Nearest-neighbor 3-band TB model (left) and up to third-nearest-neighbor 3-band TB model (right) with SOC in $MoS_2$. Fermi energy is set to zero.*

For the nearest-neighbor 3-band TB model with SOC, results were only accurate at the $\pm K$ points. Including SOC shows how at this points a notorious splitting happens at the valence band, while no splitting is seen at the conduction band. Anyway, the gap between the spin-up and spin-down gap has to be smaller at these points, so this result can be considered as an example of futility. Including SOC in the up to third-nearest-neighbor 3-band TB model shows how at this points a splitting happens at the valence band, while no splitting is seen at the conduction band. This splitting is lower that the one in the nearest-neighbor model, which reflects the accuracy of this model since SOC splitting is in the order of $10^{-1}\,(eV)$ [28]. A wider separation is found between valence and conduction band pairs, which is also a good sympton if compared with the GGA results in [18].

One expects from [18,28] that the conduction band has a splitting, but this is not found in these calculations, even performing a numerical check. It is related to the influence of the rest of orbitals that are not considered here[23]. However, the conduction band splitting is approximately

[23] A better approach can be obtained by a 5-band model which also includes the $E''$; unsatisfactory, the lack of

one order of magnitude lower in the conduction band, and TB models use to give rise to these null splittings. A more insatisfactory result is found when computing the SOC model for $WS_2$:

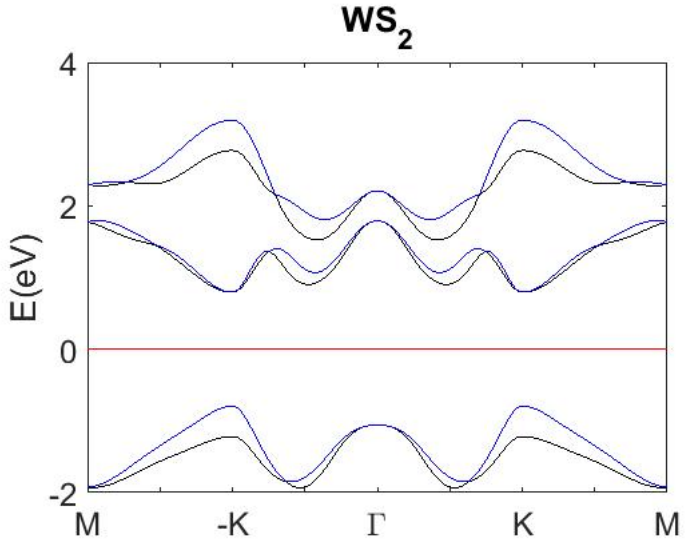


Figure 15: *Up to third-nearest-neighbor 3-band TB model with SOC in $WS_2$ . Results of interest are found at $\pm K$. Including SOC shows how at this points a splitting happens at the valence band, while no splitting is observed at the conduction band. Femi energy is set to zero.*

A null splitting is shown and calculated numericaly at $\pm K$ in the conduction band. As explained above, this is a consequence of the TB approximation. However, it is experimentally known that in $MoS_2$ there is a splitting where the spin-up conduction band is lower in energy that the spin-down conduction band at $K$. This splitting changes its sign at $-K$. The same happens in $WS_2$ but in an inverse way; the spin-up conduction band is higher in energy than the spin-down conduction band at $K$ and the splitting changes sign at $-K$. This cannot be seen in Figure 15. The valence band shows a better behaviour since one is able to compute that the valence band splitting is $\mid \triangle^v_{SOC} \mid = 0.146\,(eV)$ in $MoS_2$ while $\mid \triangle^v_{SOC} \mid = 0.422\,(eV)$, which agrees with [28]. However one should have found that the spin-down valence band at $-K$ to be higher in energy that the spin-up valence band, while the opposite should happen at $K$ for both $MoS_2$ and $WS_2$ [18].

## 4.2 $\mathbb{Z}_2$ invariant calculation in TMDC's

A theoretical introduction on the $\mathbb{Z}_2$ invariant has been developed in Chapter 2. Eq. (2.47) is the one these calculations have been based on. A rectangular path has been integrated as shown below:

ab initio information about their hopping amplitudes prevents this calculation.

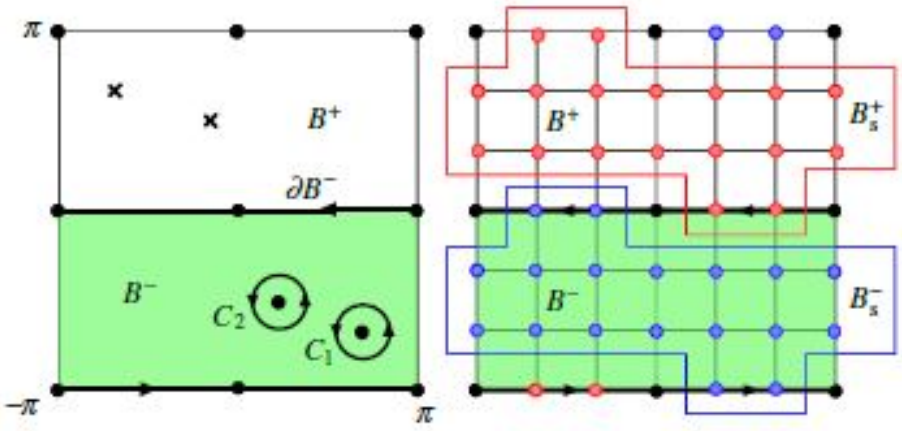


Figure 16: *Schematic representacion of the region integrated following eq. (2.47) [31]. One can chose either the green-shaded region or the white one. A summation through the contour of the region has been performed in order to integrate the Berry connection while a summation of the grid squares was performed for the Berry curvature.*

In fact, the method presented here is valid for $2D$ systems (which have 4 independent TRIM's) [31]. It must be noted that a system is a TI if the number of zeros of the pfaffian in half the 1BZ is $1 mod\,(2)$ while a conventional insulator otherwise. This is the $\mathbb{Z}_2$ invariant. A line and surface integration of the green shaded region in Figure 16 has been performed following eq. (2.47) and [31]. A result was found for every TMDC: $\mathbb{Z}_2 = 0$ [24]. This is a consequence of the opposite Berry curvature at the points $K$ and $-K$ that will be calculated in the next section, and is related to the TRS and the broken inversion symmetry as explained in Chapter 2. This shows that a trivial topological invariant can led to interesting non-trivial physics such as valley-dependent phenomena since the Berry curvature can take (locally) different non-zero values.

## 4.3 Valleytronics in TMDC's

As discussed in Chapter 2, TRS materials with broken inversion symmetry have a (locally) non-zero Berry curvature. In TMDC's this rupture of the inversion symmetry is due to the non-centrosymmetric nature of the honeycomb lattice [32]. This guarantees the Berry curvature to be odd. The Berry curvature at $\pm K$ has opposite values, which is related to the opposite sign of the anomalous velocity of the charge carriers at each valley. This fact makes each carrier to cancel each other's contribution to the Hall current. The interestinf fact of TMDC's in relation to valleytronics is that one can selectively populate valleys by valley polarization, since the separation in momentum space between $\pm K$ points supresses the intervalley scattering possibility[25]. This is achieved by populating a valley with excitons by means of circularly polarized light. Since valley-selective circular dicroism is present, this can lead to a non-vanishing charge carrier population in one valley, which is translated into a magnetization and a Valley Hall Effect

[24] These calculations have been performed through the main code developed in this research.
[25] In fact this allows the valley index $\tau = \pm 1$ to be a good quantum number.

with no need of an external magnetic field source. It is important that the mean lifetime of this exciton is greater that the mean measurement time, which constitutes a hard experimental task. The Berry curvature has been computed for different TMDC's by implementing eq. (2.15). A different approach can be used by means of eq. (2.12), but it is computationally quite time-consuming. It is important to note that the Berry curvature implemented is based in the up to third-nearest-neighbor model, where no SOC is considered. The calculation for $MoS_2$ is shown below[26]:

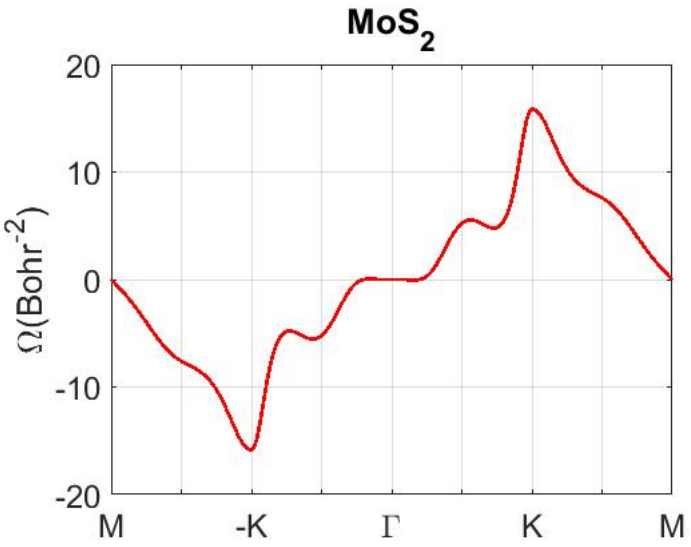


Figure 17: *Berry curvature calculation in $MoS_2$ across the path $M \longrightarrow -K \longrightarrow \Gamma \longrightarrow K \longrightarrow M$ in the frame of the up to third-neighbor hoppings 3-band TB model.*

The values at $\pm K$ are opposite, and thus a valley-dependent phenomena can occur if we populate one of the valleys with the appropiate circularly polarized light. In order to study this a degree of optical polarization can be defined as

$$\eta = \frac{\mid P_{+}^{cv}(\mathbf{k}) \mid^2 - \mid P_{-}^{cv}(\mathbf{k}) \mid^2}{\mid P_{+}^{cv}(\mathbf{k}) \mid^2 + \mid P_{-}^{cv}(\mathbf{k}) \mid^2} \tag{4.3}$$

where $P^{cv}(\mathbf{k})$ stands for $\langle u_{c\mathbf{k}} | \hat{v} | u_{v\mathbf{k}} \rangle$. In the case of circular polarized light, one shall define the polarization in terms of left-handed or right handed polarization as

$$P_{\pm}^{cv}(\mathbf{k}) = \frac{1}{\sqrt{2}} \left[ P_x^{cv} \pm i P_y^{cv} \right] \tag{4.4}$$

where

$$P_{x/y}^{cv} = \langle u_{c\mathbf{k}} | \hat{v}_{x/y} | u_{v\mathbf{k}} \rangle \tag{4.5}$$

[26]You can find in Appendix C the calculations for the rest of TMDC's.

The following result is found for the degree of circular polarization in $MoS_2$:

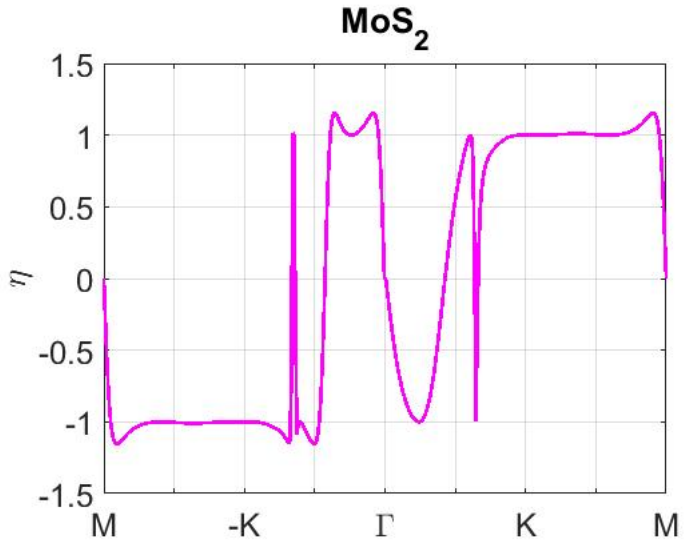


Figure 18: *Degree of circular polarization $\eta$ calculation in $MoS_2$ across the path $M \longrightarrow -K \longrightarrow \Gamma \longrightarrow K \longrightarrow M$ in the frame of the up to third-neighbor hoppings 3-band TB model.*

The highest degree of polarization is found at $\pm K$ points, and stability is shown around these points in the 1BZ. The degree of polarization is found to be high at every region in the plotted domain. In fact, values around $\pm K$ are accurate while a null polarization is found at $\Gamma$, which should not be if compared with [33]. However, since GGA calculations [18] are also different at these region, these spurious results are expected. The important valley-dependent behaviour is found at the $\pm K$ points and its experimental possibilities are proven.

# 5 ARMCHAIR GRAPHENE NANORIBBONS (AGNR's): TOPOLOGICAL PROPERTIES

Graphene nanoribbons (GNR's) are quasi-1D systems where dangling $\sigma$ orbitals are passivated so the relevant orbitals are $\pi$-like (this approach is enough for our purposes). GNR's may have two shapes depending on the cutting direction in order to prepare them which are the following ones:

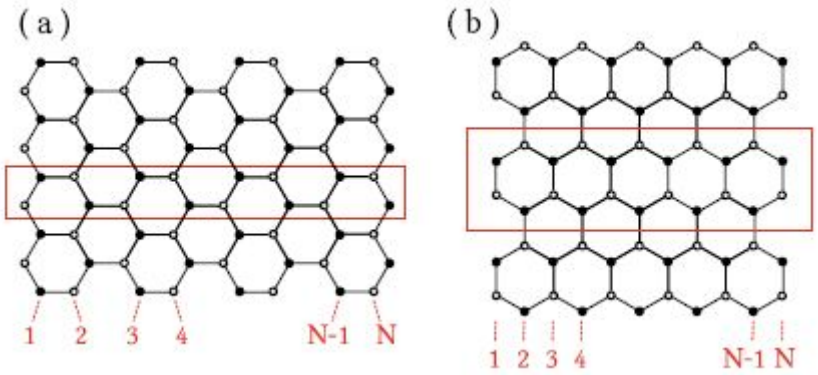


Figure 19: *Two prototypical shapes for GNR's [34]. a) A zizgag graphene nanoribbon (ZGNR) where the unit cell is depicted by a rectangle. N defines the number of zigzag lines in the unit cell. b) An armchair graphene nanoribbon (AGNR). A different unit cell is depicted by a rectangle, where N stands for the number of dimer lines inside.*

A 30$^o$ difference exists between the AGNR and the ZGNR edges[27]. This work is devoted to AGNR's. In order to calculate the band structure one has to impose open boundary conditions, whose consequences are crucial to obtain non-trivial topological phases.

Since topology is related to symmetries in the 1BZ, trivial and non-trivial topologies appear for different conditions which depend on the parity symmetry present in the AGNR's. In this study a calculation of the band structure has been performed for different $N$ values, as well as a topological characterization following [23]. A TB hamiltonian as $h(\mathbf{k})$ in graphene is used for $\pi$ orbitals with only nearest-neighbor interactions with vanishing on-site energies. One is able to write it as a 2-band hamiltonian as

$$\mathbf{h}\left(\mathbf{k}\right)\cdot\boldsymbol{\sigma}=h(\mathbf{k})=\begin{pmatrix}0 & h_x-ih_y\\ h_x+ih_y & 0\end{pmatrix} \tag{5.1}$$

where

$$h_x=1+2cos(\frac{\sqrt{3}}{2}k_xa)cos\left(\frac{1}{2}k_ya\right) \tag{5.2}$$

$$h_y=2sin(\frac{\sqrt{3}}{2}k_xa)cos(\frac{1}{2}k_ya) \tag{5.3}$$

[27] More complex shapes can be obtained from this 2 basic shapes, which is out of the scope of this work.

The eigenstates are found to be

$$u_{\pm}(\mathbf{k}) = \frac{1}{\sqrt{2}} \begin{pmatrix} e^{-i\phi(\mathbf{k})} \\ \mp 1 \end{pmatrix} \tag{5.4}$$

with $e^{-i\phi(\mathbf{k})} = \frac{h_x - ih_y}{|\mathbf{h}(\mathbf{k})|}$.

In order to obtain open boundary conditions, one has to define the general hamiltonian eigenstates as a linear combination of Bloch waves where one has to combine $\mathbf{k} = (k_x, k_y)$ and $\mathbf{k} = (k_x, -k_y)$, since periodicity is along the $x$ axis. Thus, a general expression can be the following:

$$|u_n(\mathbf{k})\rangle = \frac{1}{\sqrt{2}} \left( |u_n(k_x, k_y)\rangle - |u_n(k_x, -k_y)\rangle \right) \tag{5.5}$$

where $|u_n(k_i, k_j)\rangle$ are the Bloch waves, whose exponential terms are the ones that will give us the quantization condition. Since one can write eq. (5.5) as

$$|u_n(\mathbf{k})\rangle = \frac{1}{\sqrt{2}} \sum_j e^{ik_x x_j} \left( e^{ik_y y_j} - e^{-ik_y y_j} \right) |\phi(\mathbf{R}_j)\rangle \tag{5.6}$$

the following quantization is obtained, since $e^{ik_y y_j} - e^{-ik_y y_j} = 2isin(k_y y_j)$:

$$n\pi = \frac{(N+1)a}{2} k_y \longleftrightarrow k_y = \frac{2n\pi}{(N+1)a} \tag{5.7}$$

The $n$ determines the position (in a vertical sense) in the AGNR.

In order to study the topology of the AGNR, the argument in [23] is followed. Remember that Zak's phase is related in 1D systems to the topological invariant $\mathbb{Z}_2$ as $e^{i\sum_n \gamma_n} = (-1)^{\mathbb{Z}_2}$, where one can compute $(-1)^{\mathbb{Z}_2}$ as the product of the eigenvalues of the parity operator at the high symmetry points $\Gamma$ and $X$; that is

$$(-1)^{\mathbb{Z}_2} = \prod_n P_n(\Gamma) P_n(X) \tag{5.8}$$

Thus, the goal is to obtain the parity operator eigenvalues at the given points. In order to do so, one has to first obtain the eigenstates of the TB model, which are given, after some algebra, by

$$|u_n(\mathbf{k})\rangle = \frac{1}{\sqrt{N}} \begin{pmatrix} ie^{-i\frac{\sqrt{3}}{2}k_x a} sin\left(\frac{1}{2}k_y a\right) \\ ie^{-i\phi(\mathbf{k})} e^{-i\frac{\sqrt{3}}{2}k_x a} sin\left(\frac{1}{2}k_y a\right) \\ ie^{-i\phi(\mathbf{k})} sin(k_y a) \\ ... \end{pmatrix} \tag{5.9}$$

Let us first evaluate the eigenstate at the high-symmetry point $\Gamma$. By substitution in eq. (5.2) and eq. (5.3) one finds $h_x(\Gamma) = 1 + 2cos\left(\frac{n\pi}{N+1}\right)$ and $h_y(\Gamma) = 0$. A subtlety has to be considered when calculating $e^{-i\phi(\Gamma)}$, since $h_x$ can be either positive or negative depending on $n$ (so it depends on the AGNR arrow we are considering). A limit is found for $n = \frac{2(N+1)}{3}$, so one concludes that

$$e^{-i\phi(\Gamma)} = \begin{cases} 1 & n < \frac{2(N+1)}{3} \\ -1 & n > \frac{2(N+1)}{3} \end{cases} \tag{5.10}$$

and thus the eigenstates can be expressed as

$$|u_n(\Gamma)\rangle = \frac{1}{\sqrt{N}} \begin{pmatrix} isin\left(\frac{n\pi}{N+1}\right) \\ \pm isin\left(\frac{n\pi}{N+1}\right) \\ \pm isin\left(\frac{2n\pi}{N+1}\right) \\ ... \end{pmatrix} \tag{5.11}$$

These are also eigenstates of the parity operator, so $P_n(\Gamma)|u_n(\Gamma)\rangle = \pm|u_n(\Gamma)\rangle$ and thus, denoting the eigenvalues by $\lambda_n$, one obtains

$$\prod \lambda_n = (-1)^m \tag{5.12}$$

for $N = 3m$, $N = 3m+1$ and[28] $N = 3M+2$.

A more subtle calculation has to be performed for the $X$ point. In this case one has $h_x(X) = 1$ and $h_y(X) = 2cos\left(\frac{n\pi}{N+1}\right)$, so then

$$e^{-i\phi(X)} = \frac{1 - 2icos\left(\frac{n\pi}{N+1}\right)}{\sqrt{1 + 4cos^2\left(\frac{n\pi}{N+1}\right)}} \tag{5.13}$$

A problem arises because

$$|u_n(X)\rangle = \frac{1}{\sqrt{N}} \begin{pmatrix} sin\left(\frac{n\pi}{N+1}\right) \\ -e^{-i\phi(X)} sin\left(\frac{n\pi}{N+1}\right) \\ e^{-i\phi(X)} isin\left(\frac{2n\pi}{N+1}\right) \\ ... \end{pmatrix} \tag{5.14}$$

is not an eigenstate of the parity operator. Instead, one can see that band $n$ and $N+1-n$ are orthogonal and can be stablished by an unitary transformation as opposite parity partners at $X$, so its eigenvalues product gives $-1$. We can find by inspection that the bands for $n$ and $N+1-n$ are double degenerate for an even $N$ while for an odd $N$ there is an only degenerate band, which happens for $n = \frac{N+1}{2}$.

The product of the parity eigenvalues at the high symmetry points is given by

$$\prod \lambda_n(\Gamma)\lambda_n(X) = (-1)^{\left\lfloor \frac{N}{3} \right\rfloor} (-1)^{\left\lfloor \frac{N+1}{2} \right\rfloor} \tag{5.15}$$

[28] The latter is more complicated. For $N = 3M+2$ no gap is found in this simplified TB model, but DFT calculations show that a gap exists even for this $N$, which also fulfills eq. (5.12).

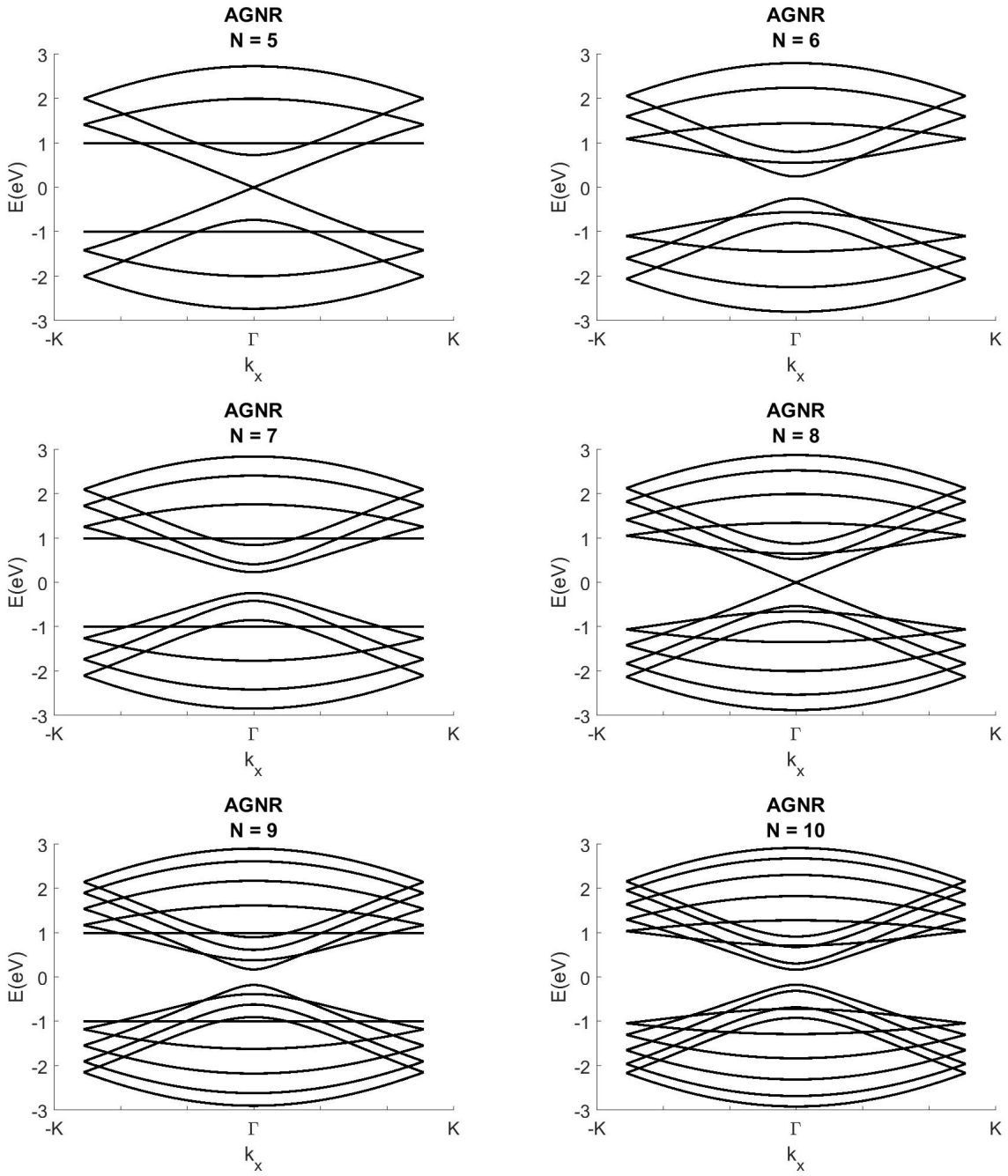


Figure 20: *AGNR band structure with* $N \in \{5, 6, 7, 8, 9, 10\}$ *along the path* $-K \longrightarrow \Gamma \longrightarrow K$.

Note that the exponents contain the floor function (it is not a modulus). Thus one can conclude after some algebra that the $\mathbb{Z}_2$ has the following expressions for even and odd $N$ (only zigzag terminations are considered here, although bearded ones could also be of interest):

$$\mathbb{Z}_2 = \frac{1-(-1)^{\lfloor \frac{N}{3} \rfloor + \lfloor \frac{N+1}{2} \rfloor}}{2} \tag{5.16}$$

$$\mathbb{Z}_2 = \frac{1+(-1)^{\lfloor \frac{N}{3} \rfloor + \lfloor \frac{N+1}{2} \rfloor}}{2} \tag{5.17}$$

A band structure calculation has been finally performed for different $N$ values from 5 to 10 in Figure 20. It can be inferred that a gapped electronic structure is observed for $N = 3p$ and $N = 3p + 1$ with $p \in \mathbb{N}$, while a gapless behavior appears for $N = 3p + 2$. We can set the following $\mathbb{Z}_2$ index classification:

$$N = 5, 6, 7, 9 \longrightarrow \mathbb{Z}_2 = 1 \tag{5.18}$$

$$N = 8, 10 \longrightarrow \mathbb{Z}_2 = 0 \tag{5.19}$$

The appearance of edge states for $N = 5$ and $N = 8$ is remarkable. For $N = 5$ edge states appear and $\mathbb{Z}_2 = 1$. However we can see that, following the arguments that gave rise to eq. (5.16) and eq. (5.17), although $N = 8$ seems to have edge states, $\mathbb{Z}_2 = 0$. The topology for the cases in eq. (5.18) and eq. (5.19) has been proven with DFT according to [23]. The number of end states at the AGNR termination is even for a trivial topology and odd for a non-trivial one. In addition, the number of localized end states uses to increase with $N$. The topological phases are protected by spatial symmetries. It seems reasonable trying to change the associated end states by breaking these symmetries at the terminating unit cells in order to induce a topological transition. An example is the $N = 7$ AGNR as argued in [23]. Note that for $N < 7$ the midgap is in the order of the $eV$, so it would be even harder to perturbate the gap. Its topological invariant is $\mathbb{Z}_2 = 1$, and this AGNR has one end state at each termination. Local perturbations from 0 $eV$ to 4 $eV$ are not enough to destroy the end states as discussed in [23], which seems to prove the robustness of the topological phase.

# 6 CONCLUSIONS

This research has focused on the band structure and the topological properties of TMDC's. A detailed theoretical introduction has been performed in order to show the utilities of topology in condensed matter physics without the topological band theory formalism, which is out of the scope of this text. A historical point of view has been followed during the three first chapters. A theoretical study on TMDC's has been performed with the preceeding knowledge. Several TB band structure calculations have been performed for different TMDC's with different levels of accuracy. A nearest-neighbor approach showed a good agreement with GGA calculations at the $\pm K$ points for some materials where a direct gap and well-defined valleys appeared, while a different behavior with an indirect gap and bad-defined valleys arose for some other TMDC's. A non-accurate behavior was found for regions far from the $\pm K$ points as well as a narrow gap was found for every TMDC. A more accurate version was calculated through an up to third-neighbor model by which well-defined direct gaps and valleys where found at the $\pm K$ points as well as a wider gap between the valence and the conduction bands. GGA calculations showed a different behavior at $\Gamma$ and $M$ points. This is a consequence of the $p$ orbitals from the chalcogen, which are not taken into account in these models. A SOC calculation has also been performed in both models. In the nearest-neighbor approach a splitting is found at the $\pm K$ points in the valence band which is not accurate with the expected values. The up to third-neighbor model shows a quite accurate splitting. In any of these models no splitting is found at the conduction band, which is a consequence of the $E''$ orbitals, whose hopping amplitudes were absent in the references. In addition a different splitting should occur at the valence bands for $MoS_2$ and $WS_2$, which is not observed due to the same reason. A calculation of the Berry curvature has been performed showing a good agreement with eq. (2.16). In addition, well-defined opposite maximum values for the Berry curvature at the $\pm K$ points are observed. This is the fundamental result of this research, which shows the possibility to selectively populate valleys with circularly polarized light in order to create excitons allowing interband transitions at these points. The degree of circular polarization also shows a maximum at the valleys and stable values around the $\pm K$ points, which strengthens these arguments.

A final calculation has been performed on AGNR's. Since graphene can be considered as a semimetal, the need to open a gap for semiconductor devices can be achieved with AGNR's. In addition, a topological study has been performed showing that for $N = 5, 6, 7, 9$ the topological phase is non-trivial while for $N = 8, 10$ it is a trivial one. The topological phases are found to be robust. An open way is then left for the study of Transition Metal Dichalcogenides Nanoribbons (TMDCNR's), which can lead to similar properties as those in graphene with a stable behavior at room temperature and a bigger gap.

### Outlook

Half of the time devoted to this research has been conditioned by the cofinement due to the Covid-19 pandemic. However, it helped to focus on this work and to devote the appropriate time. The author thinks that a wide overview on topology and physics has been offered as well as an accurate approach to valleytronics in TMDC's. A personal comment must be done. While valleytronics is a powerful tool which is thought as a complement or even as a substitute of spintronics, the lifetime of the excitons is short enough to give rise to several experimental problems. This makes another recent options to arise, such as using twisted bilayers instead of monolayers. By twisting a given angle one of the layers in the heterostructure, the exciton lifetime can be increased to 3 or 4 orders of magnitude, although the direct gap is lost. Anyhow, this field is a hot topic that seems to be very promising in the following years.

The author wants to point out that nanoribbons made up from TMDC's are the materials that can give a continuity to this research. This is a field in which the author is starting to work and seems to be a rising and promising area involving topology and (who knows yet?) even valleytronics.

# APPENDICES

## A Berry phase calculations

### A.1 Berry phase

Taking Schrödinger equation

$$i\hbar\partial_t \left|\psi\left(\mathbf{R}\right)\right\rangle = \hat{H}\left|\psi\left(\mathbf{R}\right)\right\rangle \tag{A.1}$$

and inserting eq. (2.1) and eq. (2.2) into eq. (2.3) we get:
$i\hbar\partial_t \left|\psi\left(\mathbf{R}\right)\right\rangle = i\sum_n e^{i\phi_n}\left[\partial_t c_n \left|n\left(\mathbf{R}\right)\right\rangle + c_n\partial_t \left|n\left(\mathbf{R}\right)\right\rangle + ic_n \left|n\left(\mathbf{R}\right)\right\rangle \partial_t\phi_n\right] =$

$$= \sum_n e^{i\phi_n} c_n \hat{H}\left|n\left(\mathbf{R}\right)\right\rangle \tag{A.2}$$

Since

$$i\sum_n e^{i\phi_n}\left[ic_n \left|n\left(\mathbf{R}\right)\right\rangle \partial_t\phi_n\right] = \sum_n e^{i\phi_n} c_n E_n \left|n\left(\mathbf{R}\right)\right\rangle =$$

$$= \sum_n e^{i\phi_n} c_n \hat{H}\left|n\left(\mathbf{R}\right)\right\rangle \tag{A.3}$$

it is simplified as follows:

$$i\sum_n e^{i\phi_n}\left[\partial_t c_n \left|n\left(\mathbf{R}\right)\right\rangle + c_n\partial_t \left|n\left(\mathbf{R}\right)\right\rangle\right] = 0 \tag{A.4}$$

Applying $\left\langle m\left(\mathbf{R}\right)\right|$ and considering orthonormality:

$$\sum_n e^{i\phi_n}\delta_{mn}\partial_t c_n = -\sum_n e^{i\phi_n} c_n \left\langle m\left(\mathbf{R}\right)\right| \partial_t \left|n\left(\mathbf{R}\right)\right\rangle \neq 0 \Longrightarrow m = n; \tag{A.5}$$

$$\partial_t c_m = -\sum_n c_n \left\langle m\left(\mathbf{R}\right)\right| \partial_t \left|n\left(\mathbf{R}\right)\right\rangle e^{i(\phi_n - \phi_m)} \tag{A.6}$$

Derivating on Schrödinger equation

$$\partial_t\hat{H}\left|n\left(\mathbf{R}\right)\right\rangle + \hat{H}\partial_t \left|n\left(\mathbf{R}\right)\right\rangle = \partial_t E_n \left|n\left(\mathbf{R}\right)\right\rangle + E_n\partial_t \left|n\left(\mathbf{R}\right)\right\rangle \tag{A.7}$$

and applying $\left\langle m\left(\mathbf{R}\right)\right|$ again

$$\left\langle m\left(\mathbf{R}\right)\right| \partial_t\hat{H}\left|n\left(\mathbf{R}\right)\right\rangle + \left\langle m\left(\mathbf{R}\right)\right| \hat{H}\partial_t \left|n\left(\mathbf{R}\right)\right\rangle =$$

$$= \partial_t E_n\delta_{mn} + E_n \left\langle m\left(\mathbf{R}\right)\right| \partial_t \left|n\left(\mathbf{R}\right)\right\rangle \longleftrightarrow$$

$$\longleftrightarrow \langle m(\mathbf{R})| \partial_t \hat{H} |n(\mathbf{R})\rangle + E_m \langle m(\mathbf{R})| \partial_t |n(\mathbf{R})\rangle =$$

$$= E_n \langle m(\mathbf{R})| \partial_t |n(\mathbf{R})\rangle \longleftrightarrow \{n \neq m\} \longleftrightarrow$$

$$\longleftrightarrow \langle m(\mathbf{R})| \partial_t \hat{H} |n(\mathbf{R})\rangle = (E_n - E_m) \langle m(\mathbf{R})| \partial_t |n(\mathbf{R})\rangle \longleftrightarrow$$

$$\longleftrightarrow \langle m(\mathbf{R})| \partial_t |n(\mathbf{R})\rangle = \frac{\langle m(\mathbf{R})| \partial_t \hat{H} |n(\mathbf{R})\rangle}{(E_n - E_m)} \tag{A.8}$$

we now substitute into $\partial_t c_m$ to obtain the coefficients:

$$\partial_t c_m = -\sum_{n,m} c_n \langle m(\mathbf{R})| \partial_t |n(\mathbf{R})\rangle e^{i(\phi_n - \phi_m)} =$$

$$= -\sum_{n=m} c_m \langle m(\mathbf{R})| \partial_t |n(\mathbf{R})\rangle -$$

$$-\sum_{n\neq m} c_n \frac{\langle m(\mathbf{R})| \partial_t \hat{H} |n(\mathbf{R})\rangle}{(E_n - E_m)} e^{i(\phi_n - \phi_m)} \tag{A.9}$$

Performing the adiabatic approximation

$$\frac{\langle m(\mathbf{R})| \partial_t \hat{H}(t) |n(\mathbf{R})\rangle}{(E_n - E_m)} \ll 1 \tag{A.10}$$

$\partial_t c_m$ is converted to the following:

$$\partial_t c_m \simeq -\sum_{n=m} c_m \langle m(\mathbf{R})| \partial_t |n(\mathbf{R})\rangle \longleftrightarrow c_m = \sum_{n=m} c_{0,m} e^{i\gamma_m} \tag{A.11}$$

where

$$\gamma_m = i \int \langle m(\mathbf{R})| \partial_{t'} |m(\mathbf{R})\rangle \, dt' \tag{A.12}$$

is the Berry phase. Note that since $m$ is a dummy index, we can also write (as in the main text)

$$\gamma_n = i \int \langle n(\mathbf{R})| \partial_{t'} |n(\mathbf{R})\rangle \, dt' \tag{A.13}$$

## A.2 Alternative form of the Berry curvature

Derivating the Schrödinger equation in terms of the parameter $\mathbf{R}$:

$$\boldsymbol{\partial}_{\mathbf{R}} \hat{H}(\mathbf{R}) |n(\mathbf{R})\rangle + \hat{H}(\mathbf{R}) |\boldsymbol{\partial}_{\mathbf{R}} n(\mathbf{R})\rangle = E_n |\boldsymbol{\partial}_{\mathbf{R}} n(\mathbf{R})\rangle \tag{A.14}$$

If we take the adjoint of the previous equation and multiply by $|n'(\mathbf{R})\rangle$ on the right of both sides we get the following:
$\langle n(\mathbf{R})|\,\boldsymbol{\partial}_{\mathbf{R}}\hat{H}(\mathbf{R})\,|n'(\mathbf{R})\rangle + \langle\boldsymbol{\partial}_{\mathbf{R}}n(\mathbf{R})|\,\hat{H}(\mathbf{R})\,|n'(\mathbf{R})\rangle = E_n\langle\boldsymbol{\partial}_{\mathbf{R}}n(\mathbf{R})\,|n'(\mathbf{R})\rangle \longleftrightarrow$

$$\longleftrightarrow \langle n(\mathbf{R})|\,\boldsymbol{\partial}_{\mathbf{R}}\hat{H}(\mathbf{R})\,\big|n'(\mathbf{R})\big\rangle = (E_n - E_{n'})\,\big\langle\boldsymbol{\partial}_{\mathbf{R}}n(\mathbf{R})\,\big|n'(\mathbf{R})\big\rangle \tag{A.15}$$

We can identify $\langle\boldsymbol{\partial}_{\mathbf{R}}n(\mathbf{R})\,|n'(\mathbf{R})\rangle$ as the adjoint of a Berry connection. Considering the same for $\left\langle n'(\mathbf{R})\,|\boldsymbol{\partial}_{\mathbf{R}}n(\mathbf{R})\right\rangle$ and summing over $n'$ to obtain completeness
$\Omega^n_{\mu\nu}(\mathbf{R}) = i\sum_{n'\neq n}\left[\langle\partial_\mu n(\mathbf{R})\,|n'(\mathbf{R})\rangle\langle n'(\mathbf{R})\,|\partial_\nu n(\mathbf{R})\rangle - \langle\partial_\nu n(\mathbf{R})\,|n'(\mathbf{R})\rangle\langle n'(\mathbf{R})\,|\partial_\mu n(\mathbf{R})\rangle\right]$
we get

$$\Omega^n_{\mu\nu}(\mathbf{R}) = i\sum_{n'\neq n}\left[\frac{\langle n(\mathbf{R})|\,\partial_\mu\hat{H}(\mathbf{R})\,|n'(\mathbf{R})\rangle\langle n'(\mathbf{R})|\,\partial_\nu\hat{H}(\mathbf{R})\,|n(\mathbf{R})\rangle - c.c}{(E_n - E'_n)^2}\right] \tag{A.16}$$

## A.3 Electron velocity under adiabatic perturbations

Computing the expectacion value of the velocity in the new basis, this is what we find:
$\left\langle u'_n(\mathbf{k},t)\right|\frac{1}{\hbar}\partial_{\mathbf{q}}\hat{H}(\mathbf{k},t)\left|u'_n(\mathbf{k},t)\right\rangle = \langle u_n(\mathbf{k},t)|\,\frac{1}{\hbar}\partial_{\mathbf{q}}\hat{H}(\mathbf{k},t)\,|u_n(\mathbf{k},t)\rangle -$

$$-i\sum_{n\neq n'}\left[\frac{\langle u_n(\mathbf{k},t)|\,\partial_{\mathbf{q}}\hat{H}(\mathbf{k},t)\left|u'_n(\mathbf{k},t)\right\rangle\left\langle u'_n(\mathbf{k},t)\right|\partial_t u_n(\mathbf{k},t)\right\rangle}{E_n - E_{n'}} - h.c\right] \tag{A.17}$$

The first term is clearly $\frac{1}{\hbar}\partial_{\mathbf{k}}E_n(\mathbf{k})$. In the second one, taking into accout the relation

$$\langle u_n(\mathbf{k},t)|\,\partial_{\mathbf{k}}\hat{H}(\mathbf{k},t)\,|u_{n'}(\mathbf{k},t)\rangle = (E_n - E_{n'})\left\langle\partial_{\mathbf{k}}u_n(\mathbf{k},t)\,|u_{n'}(\mathbf{k},t)\right\rangle \tag{A.18}$$

we are able to rewrite it as

$$-i\sum_{n\neq n'}\left[\left\langle\partial_{\mathbf{k}}u_n(\mathbf{k},t)\,|u_{n'}(\mathbf{k},t)\rangle\langle u_{n'}(\mathbf{k},t)|\,\partial_t u_n(\mathbf{k},t)\right\rangle - h.c\right] \tag{A.19}$$

obtaining the Berry curvature. Thus, a general final result can be given for the expectation value of the velocity operator in $\mathbf{k}$-space as

$$\left\langle u'_n(\mathbf{k},t)\right|\hat{v}(\mathbf{k})\left|u'_n(\mathbf{k},t)\right\rangle = \frac{1}{\hbar}\partial_{\mathbf{k}}\mathbf{E}_{\mathbf{n}}(\mathbf{k}). - \Omega^n_{\mathbf{k}t} \tag{A.20}$$

## A.4 TR polarization

One can choose a matrix representation for the time-reversal operator [35] in terms of the Bloch states as

$$w_{\alpha\beta}(u_{n\mathbf{k}}) = \langle u_{\alpha,-\mathbf{k}}|\,T\,|u_{\beta,\mathbf{k}}\rangle \tag{A.21}$$

It is not hard to notice that $w$ is antisymmetric so $w_{\beta\alpha}(-\mathbf{k}) = -w_{\alpha\beta}(\mathbf{k})$. For a 2-band model (where a single Kramer's pair will exist) it is found

$$\sum_{\alpha,\beta} \langle u_{\alpha,-\mathbf{k}}| \hat{T} |u_{\beta,\mathbf{k}}\rangle = \begin{pmatrix} u_{1,-\mathbf{k}} & u_{2,-\mathbf{k}} \end{pmatrix} \begin{pmatrix} Tu_{1,\mathbf{k}} \\ Tu_{2,\mathbf{k}} \end{pmatrix} = \begin{pmatrix} 0 & w_{12} \\ -w_{12} & 0 \end{pmatrix} \tag{A.22}$$

Since this a time reversal operator representation, one can try to find a expression which relates TRS with another object. In the case of the Berry potential the following is found:

$$A(-\mathbf{k}) = w(\mathbf{k}) A^*(\mathbf{k}) w^\dagger(\mathbf{k}) + iw(\mathbf{k}) \partial_{\mathbf{k}} w^\dagger(\mathbf{k}) \tag{A.23}$$

$$Tr[A(-\mathbf{k})] = Tr[A^*(\mathbf{k})] + i \cdot Tr\left[w(\mathbf{k}) \partial_{\mathbf{k}} w^\dagger(\mathbf{k})\right] \tag{A.24}$$

From

$$Tr[A] = Tr[A^*] \tag{A.25}$$

and

$$w(\mathbf{k}) \partial_{\mathbf{k}} w^\dagger(\mathbf{k}) = -[\partial_{\mathbf{k}} w(\mathbf{k})] w^\dagger(\mathbf{k}) \tag{A.26}$$

one finds

$$Tr[A(\mathbf{k})] = Tr[A(-\mathbf{k})] + i \cdot Tr\left[w^\dagger(\mathbf{k}) \partial_{\mathbf{k}} w(\mathbf{k})\right] \tag{A.27}$$

At this point it is compulsory to introduce the charge polarizations, constituted by a total polarization $P_\rho = P_1 + P_2$ and a time-reversal polarization $P_\theta = P_1 - P_2$. The latter describes the charge polarization difference between a spin-up and a spin-down band. The TR operator acts on the bands as follows:

$$T|u_2(\mathbf{k})\rangle = e^{-i\chi(\mathbf{k})} |u_1(-\mathbf{k})\rangle \tag{A.28}$$

$$T|u_1(\mathbf{k})\rangle = -e^{-i\chi(-\mathbf{k})} |u_2(-\mathbf{k})\rangle \tag{A.29}$$

This allows to write an explicit version of the matrix representation:

$$w(\mathbf{k}) = \begin{pmatrix} 0 & e^{-i\chi(\mathbf{k})} \\ -e^{-i\chi(-\mathbf{k})} & 0 \end{pmatrix} \tag{A.30}$$

Since the polarization charge behaves as

$$P_i = \int_{-\pi}^{\pi} \frac{dk}{2\pi} A_{ii}(k) \tag{A.31}$$

$$P_\rho = \sum P_i = P_1 + P_2 \tag{A.32}$$

the following is found in terms of the Berry connection:

$$P_1 = \frac{1}{2\pi}\left[\int_0^\pi dk \cdot A_{11}(k) + \int_{-\pi}^0 dk \cdot A_{11}(k)\right] =$$

$$= \frac{1}{2\pi}\int_0^\pi dk \cdot \left[A_{11}(k) + A_{22}(k) - \frac{d\chi(k)}{dk}\right] =$$

[29]

$$= \int_0^\pi \frac{dk}{2\pi} A(k) - \frac{1}{2\pi}\left[\chi(\pi) - \chi(0)\right] = \int_0^\pi \frac{dk}{2\pi} A(k) - \frac{i}{2\pi} ln\left[\frac{w_{12}(\pi)}{w_{12}(0)}\right] \tag{A.33}$$

Now we calculate the time-reversal polarization $P_\theta$:

$$P_\theta = 2P_1 - P_\rho = \int_0^\pi dk \left[Tr\left[A(\mathbf{k})\right] - Tr\left[A(-\mathbf{k})\right]\right] - \frac{i}{2\pi} ln\left[\frac{w_{12}(\pi)}{w_{12}(0)}\right] =$$

$$= \int_0^\pi \frac{dk}{2\pi}\left[i \cdot Tr\left[w^\dagger(\mathbf{k})\,\partial_{\mathbf{k}} w(\mathbf{k})\right]\right] - \frac{i}{\pi} ln\left[\frac{w_{12}(\pi)}{w_{12}(0)}\right] = \left\{w_{12}^2 = det(w)\right\} =$$

$$= \frac{1}{i\pi} ln\left[\frac{w(\pi)}{w(0)}\frac{\sqrt{w^2(0)}}{\sqrt{w^2(\pi)}}\right] \tag{A.34}$$

# B Topological phases calculations

## B.1 QHE with non-perturbative approach

Taking the usual gauge potential $\mathbf{A} = (0, x, 0)\,B$ and the consideration that $\mathbf{B} = \boldsymbol{\nabla} \times \mathbf{A} = B\mathbf{k}$, we can write the canonical conjugate momentum as $\mathbf{p} + \frac{e}{c}\mathbf{A}$. The hamiltonian asociated with this momentum is

$$\hat{H} = \frac{1}{2m}\left(\hat{p}_x^2 + \left(\hat{p}_y + \frac{e}{c}B\hat{x}\right)^2\right) + V \tag{B.1}$$

Given that the expectation value for the intensity is defined as

$$< I = -\frac{e}{m}\sum_{n,k} \langle\psi_{n,k}|\,\mathbf{p} + \frac{e}{c}\mathbf{A}\,|\psi_{n,k}\rangle \tag{B.2}$$

where $|\psi_{n,k}\rangle$ denotes a Bloch function for the $n$-th band, one can manipulate the last equation as follows:

$$\langle I\rangle = \langle I_x\rangle + \langle I_y\rangle \tag{B.3}$$

[29] $w_{12}(\mathbf{k}) = e^{-i\chi(\mathbf{k})} \longleftrightarrow \chi(\mathbf{k}) = i \cdot ln\left(w_{12}(\mathbf{k})\right)$

where

$$\begin{aligned}\langle I_x\rangle &= -\tfrac{e}{m}\textstyle\sum_n^\nu\sum_k \langle\psi_{n,k}| - i\hbar\partial_x |\psi_{n,k}\rangle = 0\\ \langle I_y\rangle &= -\tfrac{e}{m}\textstyle\sum_n^\nu\sum_k \left(\hbar k + \langle\psi_{n,k}| \tfrac{e}{c}xB |\psi_{n,k}\rangle\right)\end{aligned} \tag{B.4}$$

The second term can be manipulated taking into consideration that the wavefunction is not centered at $x = 0$ but at $x = \frac{mc^2E}{2B^2} - \hbar k\frac{c}{eB}$, giving rise to the following result:

$$\langle I_y\rangle = -\frac{e}{m}\sum_n^\nu\sum_k \left(\hbar k + \langle\psi_{n,k}| \frac{e}{c}xB |\psi_{n,k}\rangle\right) =$$

$$= -\frac{e}{m}\sum_n^\nu\sum_k \left(\hbar k - \hbar k + \frac{mcE}{B}\right) = -e\nu c\sum_k \frac{E}{B} \tag{B.5}$$

In order to evaluate the sum, a given geometry has to be considered. Let us think of a slab with area $A = L_xL_y$. Since invariance respect to the $y$ axis is present, periodic boundary conditions respect to this axis will lead to $\frac{2\pi}{L_y}$. The number of degenerate states for a given level is calculated as follows:

$$g = \frac{L_y}{2\pi}\int_{-\frac{L_x}{l_B^2}}^0 dk = \frac{AeB}{h} \tag{B.6}$$

Thus one finds that the expectation value for the current along the $y$ axis is:

$$\langle I_y\rangle = -e\nu c\frac{E}{B}\frac{AeB}{h} = -\frac{e^2\nu c}{h}EA \tag{B.7}$$

while the current density $j_y = \sigma_{xy}E_x$ will be

$$j_y = \frac{I_y}{A} = -\frac{e^2\nu c}{h}E \longleftrightarrow \sigma_{xy} = \frac{e^2c}{h}\nu; \nu \in \mathbb{N} \tag{B.8}$$

The previous calculations are mostly straightforward and show the quantization on the Hall conductivity by an integer $\nu$, which constitutes a topological quantum number with an enormous importance, the TKNN invariant.

## B.2 Peierls substitution

Since creation and destruction operators only affect the Wannier states, it is only necessary to study the hopping amplitudes change. A tedious algebra leads to the following result:

$$\hat{H}\,|\psi_{\mathbf{R}}\rangle = e^{i\frac{q}{\hbar}\int_{\mathbf{R}}^{\mathbf{r}}\mathbf{A}(\mathbf{r}',t)d\mathbf{r}'}\hat{H}_0\,|\psi_{\mathbf{R}}\rangle \tag{B.9}$$

The hopping amplitude will be then:

$$t'_{ij} = \langle\psi_{\mathbf{R}_i}|\,\hat{H}\,|\psi_{\mathbf{R}_j}\rangle = \langle\psi_{\mathbf{R}_i}|\,e^{i\frac{q}{\hbar}\left(\int_{\mathbf{r}}^{\mathbf{R_j}}\mathbf{A}(\mathbf{r}',t)d\mathbf{r}' - \int_{\mathbf{R_i}}^{\mathbf{r}}\mathbf{A}(\mathbf{r}',t)d\mathbf{r}'\right)}\hat{H}\,|\psi_{\mathbf{R}_j}\rangle =$$

$$= e^{i\frac{q}{\hbar}\left(\int_{\mathbf{R_i}}^{\mathbf{R_j}} \mathbf{A}(\mathbf{r}',t)d\mathbf{r}'\right)} \int e^{i\frac{q}{\hbar}\phi(\mathbf{r})}\psi\left(\mathbf{r}-\mathbf{R_i}\right) H\psi\left(\mathbf{r}-\mathbf{R_j}\right) \simeq$$

$$\simeq e^{i\frac{q}{\hbar}\left(\int_{\mathbf{R_i}}^{\mathbf{R_j}} \mathbf{A}(\mathbf{r}',t)d\mathbf{r}'\right)} \left\langle \psi_{\mathbf{R_i}} \right| \hat{H} \left| \psi_{\mathbf{R_j}} \right\rangle = e^{i\frac{q}{\hbar}\left(\int_{\mathbf{R_i}}^{\mathbf{R_j}} \mathbf{A}(\mathbf{r}',t)d\mathbf{r}'\right)} t_{ij} \tag{B.10}$$

## B.3 Haldane's model calculations

The terms in $\mathbf{h_1}$ are worked below:

$$-\left(f(\mathbf{k})te^{i\frac{q}{\hbar}\theta_{ij}} + f^*(\mathbf{k})t'e^{-i\frac{q}{\hbar}\theta_{ij}}\right) = -\sum_{j=1}^{3}\left(e^{-i\mathbf{k}\boldsymbol{\delta_j}}t'e^{i\frac{q}{\hbar}\theta_{ij}} + e^{i\mathbf{k}\boldsymbol{\delta_j}}t'e^{-i\frac{q}{\hbar}\theta_{ij}}\right) =$$

$$= -\left(e^{-i\mathbf{k}\boldsymbol{\delta_1}} + e^{-i\mathbf{k}\boldsymbol{\delta_2}} + e^{-i\mathbf{k}\boldsymbol{\delta_3}}\right)t'e^{i\frac{q}{\hbar}\theta_{ij}} - \left(e^{i\mathbf{k}\boldsymbol{\delta_1}} + e^{i\mathbf{k}\boldsymbol{\delta_2}} + e^{i\mathbf{k}\boldsymbol{\delta_3}}\right)t'e^{-i\frac{q}{\hbar}\theta_{ij}} =$$

$$= -t'\left(e^{-i\left(\mathbf{k}\boldsymbol{\delta_1}-\frac{q}{\hbar}\theta_{ij}\right)} + e^{-i\left(\mathbf{k}\boldsymbol{\delta_2}-\frac{q}{\hbar}\theta_{ij}\right)} + e^{-i\left(\mathbf{k}\boldsymbol{\delta_3}-\frac{q}{\hbar}\theta_{ij}\right)}\right) -$$

$$-t'\left(e^{i\left(\mathbf{k}\boldsymbol{\delta_1}-\frac{q}{\hbar}\theta_{ij}\right)} + e^{i\left(\mathbf{k}\boldsymbol{\delta_2}-\frac{q}{\hbar}\theta_{ij}\right)} + e^{i\left(\mathbf{k}\boldsymbol{\delta_3}-\frac{q}{\hbar}\theta_{ij}\right)}\right) =$$

$$= -2t'\left(cos\left(\mathbf{k}\boldsymbol{\delta_1} - \frac{q}{\hbar}\theta_{ij}\right) + cos\left(\mathbf{k}\boldsymbol{\delta_2} - \frac{q}{\hbar}\theta_{ij}\right) + cos\left(\mathbf{k}\boldsymbol{\delta_3} - \frac{q}{\hbar}\theta_{ij}\right)\right) \tag{B.11}$$

$$-\left(f^*(\mathbf{k})t'e^{i\frac{q}{\hbar}\theta_{ij}} + f(\mathbf{k})t'e^{-i\frac{q}{\hbar}\theta_{ij}}\right) = -\sum_{j=1}^{3}\left(e^{i\mathbf{k}\boldsymbol{\delta_j}}t'e^{i\frac{q}{\hbar}\theta_{ij}} + e^{-i\mathbf{k}\boldsymbol{\delta_j}}t'e^{-i\frac{q}{\hbar}\theta_{ij}}\right) =$$

$$= -\left(e^{i\mathbf{k}\boldsymbol{\delta_1}} + e^{i\mathbf{k}\boldsymbol{\delta_2}} + e^{i\mathbf{k}\boldsymbol{\delta_3}}\right)t'e^{i\frac{q}{\hbar}\theta_{ij}} - \left(e^{-i\mathbf{k}\boldsymbol{\delta_1}} + e^{-i\mathbf{k}\boldsymbol{\delta_2}} + e^{-i\mathbf{k}\boldsymbol{\delta_3}}\right)t'e^{-i\frac{q}{\hbar}\theta_{ij}} =$$

$$= -t'\left(e^{i\left(\mathbf{k}\boldsymbol{\delta_1}+\frac{q}{\hbar}\theta_{ij}\right)} + e^{i\left(\mathbf{k}\boldsymbol{\delta_2}+\frac{q}{\hbar}\theta_{ij}\right)} + e^{i\left(\mathbf{k}\boldsymbol{\delta_3}+\frac{q}{\hbar}\theta_{ij}\right)}\right) -$$

$$-t'\left(e^{-i\left(\mathbf{k}\boldsymbol{\delta_1}+\frac{q}{\hbar}\theta_{ij}\right)} + e^{-i\left(\mathbf{k}\boldsymbol{\delta_2}+\frac{q}{\hbar}\theta_{ij}\right)} + e^{-i\left(\mathbf{k}\boldsymbol{\delta_3}+\frac{q}{\hbar}\theta_{ij}\right)}\right) =$$

$$= -2t'\left(cos\left(\mathbf{k}\boldsymbol{\delta_1} + \frac{q}{\hbar}\theta_{ij}\right) + cos\left(\mathbf{k}\boldsymbol{\delta_2} + \frac{q}{\hbar}\theta_{ij}\right) + cos\left(\mathbf{k}\boldsymbol{\delta_3} + \frac{q}{\hbar}\theta_{ij}\right)\right) \tag{B.12}$$

The $h(\mathbf{k})$ components will be then

$$h_{11} = \varepsilon - 2t'\left(cos\left(\mathbf{k}\boldsymbol{\delta_1} - \frac{q}{\hbar}\theta_{ij}\right) + cos\left(\mathbf{k}\boldsymbol{\delta_2} - \frac{q}{\hbar}\theta_{ij}\right) + cos\left(\mathbf{k}\boldsymbol{\delta_3} - \frac{q}{\hbar}\theta_{ij}\right)\right) \tag{B.13}$$

$$h_{22} = -\varepsilon - 2t' \left( cos\left(\mathbf{k}\boldsymbol{\delta_1} + \frac{q}{\hbar}\theta_{ij}\right) + cos\left(\mathbf{k}\boldsymbol{\delta_2} + \frac{q}{\hbar}\theta_{ij}\right) + cos\left(\mathbf{k}\boldsymbol{\delta_3} + \frac{q}{\hbar}\theta_{ij}\right)\right) \tag{B.14}$$

$$h_{12} = h_{21}^{*} = -tf\left(\mathbf{k}\right) \tag{B.15}$$

### B.4 Eigenstates in Haldane's model

The eigenstates calculation is performed:

$$ker(\hat{H} - \epsilon I) \longrightarrow \begin{pmatrix} d_z + |d\left(\mathbf{k}\right)| & d_x - id_y \\ d_x + id_y & -d_z + |d\left(\mathbf{k}\right)| \end{pmatrix} \begin{pmatrix} u \\ v \end{pmatrix} = 0 \tag{B.16}$$

Using the second equation from the previous system:

$$\left(d_x + id_y\right) u - \left(d_z - |d\left(\mathbf{k}\right)|\right) v = 0 \longleftrightarrow u = v\frac{d_z - |d\left(\mathbf{k}\right)|}{d_x + id_y} \longrightarrow$$

$$|\psi_-\rangle = v \begin{pmatrix} \frac{d_z - |d(\mathbf{k})|}{d_x + id_y} \\ 1 \end{pmatrix} = \frac{v}{d_x + id_y} \begin{pmatrix} d_z - |d\left(\mathbf{k}\right)| \\ d_x + id_y \end{pmatrix} = \frac{1}{N} \begin{pmatrix} d_z - |d\left(\mathbf{k}\right)| \\ d_x + id_y \end{pmatrix} \tag{B.17}$$

Normalizing one gets $N$:

$$1 = \left\langle \psi_- \middle| \psi_- \right\rangle = \frac{1}{|N|^2} \begin{pmatrix} d_z - |d\left(\mathbf{k}\right)| & d_x - id_y \end{pmatrix} \begin{pmatrix} d_z - |d\left(\mathbf{k}\right)| \\ d_x + id_y \end{pmatrix} =$$

$$= \frac{1}{|N|^2} \left[ \left(d_z - |d\left(\mathbf{k}\right)|\right)^2 + d_x^2 + d_y^2 \right] = \frac{2d\left(\mathbf{k}\right)\left[d\left(\mathbf{k}\right) - d_z\right]}{|N|^2} \longleftrightarrow$$

$$\longleftrightarrow \frac{1}{N} = \frac{1}{2d\left(\mathbf{k}\right)\left[d\left(\mathbf{k}\right) - d_z\right]} \tag{B.18}$$

Thus, the valence band wavefunction is

$$|\psi_-\rangle = \frac{1}{2d\left(\mathbf{k}\right)\left[d\left(\mathbf{k}\right) - d_z\right]} \begin{pmatrix} d_z - |d\left(\mathbf{k}\right)| \\ d_x + id_y \end{pmatrix} \tag{B.19}$$

## C Berry curvature and circular degree of polarization calculations

The Berry curvature and circular degree of polarization for several TMDC's is shown in this appendix:

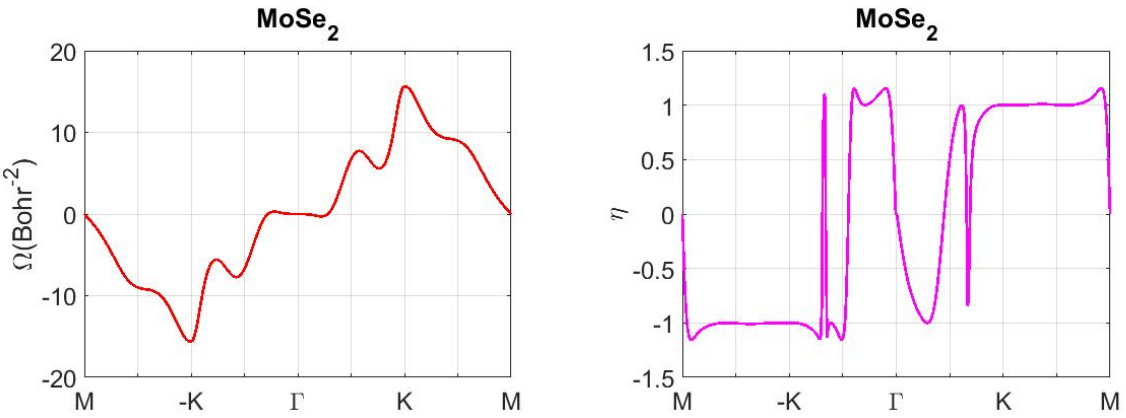


Figure 21: *Berry curvature (left) and circular degree of polarization (right) calculation in $MoSe_2$ across the path $M \longrightarrow -K \longrightarrow \Gamma \longrightarrow K \longrightarrow M$ in the frame of the up to third-neighbor hoppings 3-band TB model.*

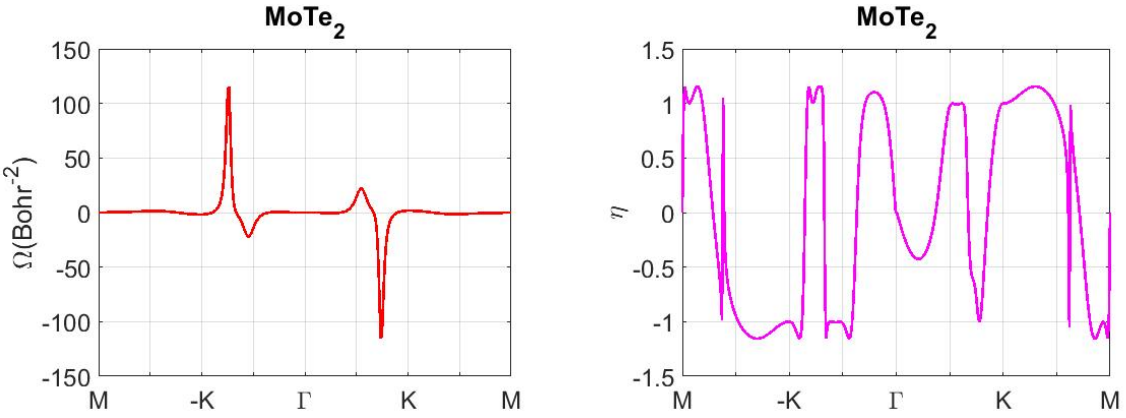


Figure 22: *Berry curvature (left) and circular degree of polarization (right) calculation in $MoTe_2$ across the path $M \longrightarrow -K \longrightarrow \Gamma \longrightarrow K \longrightarrow M$ in the frame of the up to third-neighbor hoppings 3-band TB model.*

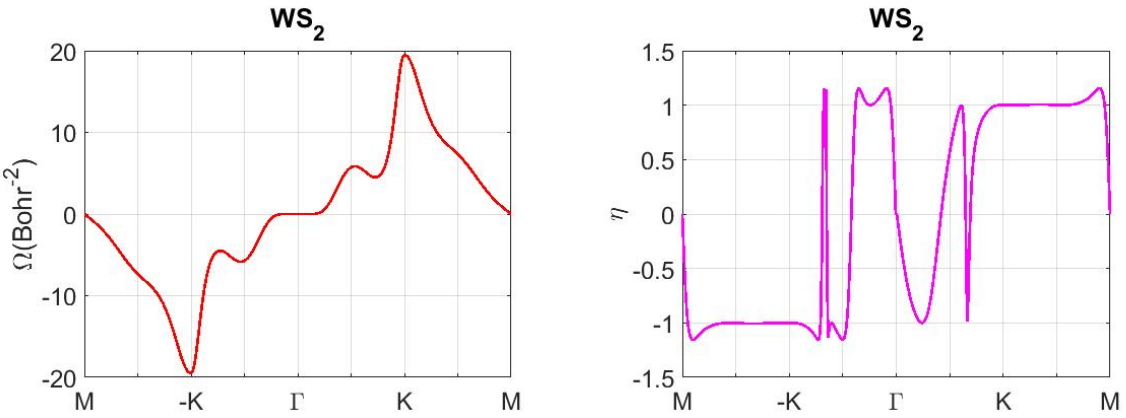


Figure 23: *Berry curvature (left) and circular degree of polarization (right) calculation in $WS_2$ across the path $M \longrightarrow -K \longrightarrow \Gamma \longrightarrow K \longrightarrow M$ in the frame of the up to third-neighbor hoppings 3-band TB model.*

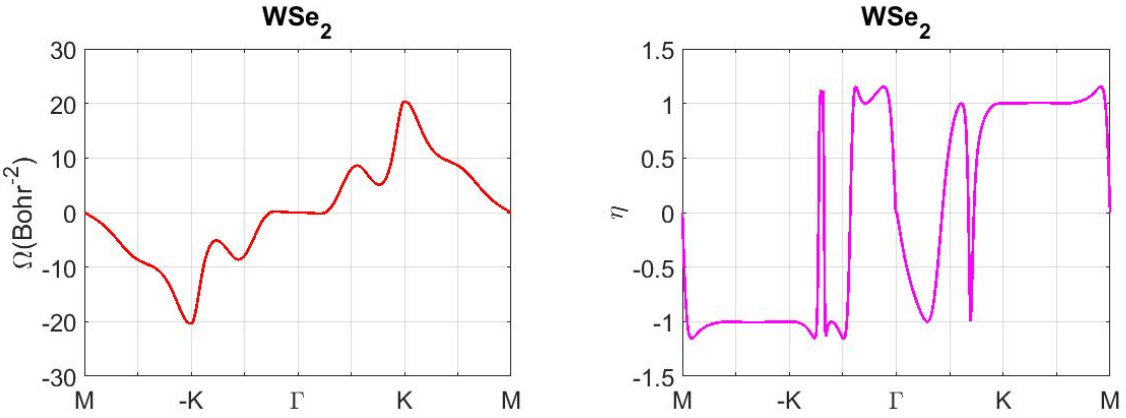


Figure 24: *Berry curvature (left) and circular degree of polarization (right) calculation in $WSe_2$ across the path $M \longrightarrow -K \longrightarrow \Gamma \longrightarrow K \longrightarrow M$ in the frame of the up to third-neighbor hoppings 3-band TB model.*

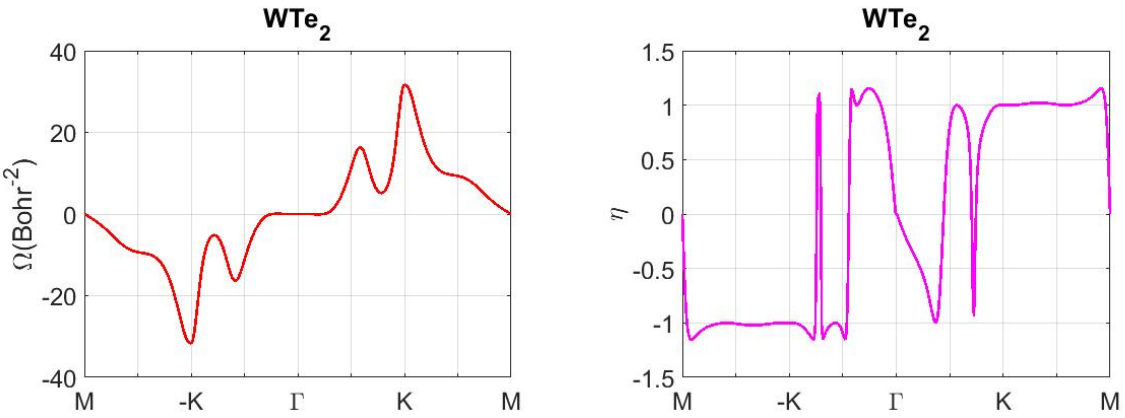


Figure 25: *Berry curvature (left) and circular degree of polarization (right) calculation in* $WTe_2$ *across the path* $M \longrightarrow -K \longrightarrow \Gamma \longrightarrow K \longrightarrow M$ *in the frame of the up to third-neighbor hoppings 3-band TB model.*

## References


[1] K. v. Klitzing, G. Dorda, and M. Pepper. *New Method for High-Accuracy Determination of the Fine-Structure Constant Based on Quantized Hall Resistance.* Phys. Rev. Lett. ***45***, 494 (1980).

[2] R. B. Laughlin. *Quantized Hall conductivity in two dimensions.* Phys. Rev. B ***23***, 5632(R) (1981).

[3] D. J. Thouless, M. Kohmoto, M. P. Nightingale and M. den Nijs. *Quantized Hall Conductance in a Two-Dimensional Periodic Potential.* Phys. Rev. Lett. ***49***, 405 (1982).

[4] D. J. Thouless. *Quantization of particle transport.* Phys. Rev. B ***27***, 6083 (1983).

[5] R. Tao and D. J. Thouless. *Fractional quantization of Hall conductance.* Phys. Rev. B ***28***, 1142(R) (1983).

[6] B. Simon. *Holonomy, the Quantum Adiabatic Theorem, and Berry's Phase.* Phys. Rev. Lett. ***51***, 2167 (1983).

[7] J. E. Avron, R. Seiler and B. Simon. *Homotopy and Quantization in Condensed Matter Physics.* Phys. Rev. Lett. ***51***, 24 (1983).

[8] M. V. Berry. *Quantal phase factors accompanying adiabatic changes.* Proc. R. Soc. London, Sec. A ***392***, 45 (1984).

[9] M. Z. Hasan and C. L. Kane. *Colloquium: Topological insulators.* Rev. Mod. Phys. ***82***, 3045 (2010).

[10] D. Xiao, M. C. Chang and Q. Niu. *Berry phase effects on electronic properties.* Rev. Mod. Phys. ***82***, 1959 (2010).

[11] J. Zak. *Berry's phase for energy bands in solids.* Phys. Rev. Lett. ***62***, 2747 (1989).

[12] M. Kohmoto. *Topological Invariant and the Quantization of the Hall Conductance.* Ann. Phys. Paris ***160***, 343 (1985).

[13] M. C. Chang and Q. Niu. *Berry Phase, Hyperorbits, and the Hofstadter Spectrum.* Phys. Rev. Lett. ***75***, 1348 (1995).

[14] G. Sundaram and Q. Niu. *Wave-packet dynamics in slowly perturbed crystals: Gradient corrections and Berry-phase effects.* Phys. Rev. B ***59***, 14915 (1999).

[15] C. L. Kane and E. J. Mele. $\mathbb{Z}_2$ *Topological Order and the Quantum Spin Hall Effect.* Phys. Rev. Lett. ***95***, 146802 (2005).

[16] C. L. Kane and E. J. Mele. *Quantum Spin Hall Effect in Graphene.* Phys. Rev. Lett. ***95***, 226801 (2005).

[17] L. Fu and C. L. Kane. *Time reversal polarization and a $\mathbb{Z}_2$ adiabatic spin pump.* Phys. Rev. B ***74***, 195312 (2006).

[18] G. B. Liu et al. *Three-band tight-binding model for monolayers of group-VIB transition metal dichalcogenides.* Phys. Rev. B ***88***, 085433 (2013).

[19] D. Xiao, W. Yao and Q. Niu. *Valley-Contrasting Physics in Graphene: Magnetic Moment and Topological Transport.* Phys. Rev. Lett. ***99***, 236809 (2007).

[20] W. Yao, D. Xiao and Q. Niu. *Valley-dependent optoelectronics from inversion symmetry breaking.* Phys. Rev. B ***77***, 235406 (2008).

[21] D. Xiao et al. *Coupled Spin and Valley Physics in Monolayers of $MoS_2$ and Other Group-VI Dichalcogenides.* Phys. Rev. Lett. ***108***, 196802 (2012).

[22] L. Fu and C. L. Kane. *Topological insulators with inversion symmetry.* Phys. Rev. B ***76***, 045302 (2007).

[23] T. Cao, F. Zhao and S. G. Louie. *Topological Phases in Graphene Nanoribbons: Junction States, Spin Centers, and Quantum Spin Chains.* Phys. Rev. Lett. ***119***, 076401 (2017).

[24] F. D. M. Haldane. *Model for a Quantum Hall Effect without Landau Levels: Condensed-Matter Realization of the "Parity Anomaly".* Phys. Rev. Lett. ***61***, 2015 (1988).

[25] M. Fruchart and D. Carpentier. *An introduction to topological insulators.* Comptes Rendus Physique ***14***, 779 (2013).

[26] J. Maciejko, T. L. Hughes and S. C. Zhang. *The Quantum Spin Hall Effect.* Annual Review of Condensed Matter Physics ***2***, 31 (2011).

[27] H. Zhang, and X. L. Q. *Topological insulators and superconductors.* Rev. Mod. Phys. ***83***, 1057 (2011).

[28] S. Manzeli et al. *2D transition metal dichalcogenides.* Nature Reviews Materials ***2***, 8, 17033 (2017).

[29] E. Cappelluti et al. *Tight-binding model and direct-gap/indirect-gap transition in single-layer and multilayer $MoS_2$.* Phys. Rev. B ***88***, 075409 (2013).

[30] S. Fang et al. *Ab initio tight-binding Hamiltonian for transition metal dichalcogenides.* Phys. Rev. B ***92***, 205108 (2015).

[31] T. Fukui and Y. Hatsugai. *Quantum Spin Hall Effect in Three Dimensional Materials: Lattice Computation of $\mathbb{Z}_2$ Topological Invariants and Its Application to Bi and Sb.* J. Phys. Soc. Jpn. ***76***, 053702 (2007).

[32] J. R. Schaibley et al. *Valleytronics in 2D materials.* Nature Reviews Materials ***1***, 16055 (2016).

[33] T. Cao et al. *Valley-selective circular dichroism of monolayer molybdenum disulphide.* Nature Comunications ***3***, 887 (2012).

[34] S. M.-M. Dubois, Z. Zanolli, X. Declerck and J. C. Charlier. *Electronic properties and quantum transport in Graphene-based nanostructures.* The European Physical Journal B ***72***, 1 (2009).

[35] Y. Ando. *Topological Insulator Materials.* J. Phys. Soc. Jpn. ***82***, 102001 (2013).

[36] P. Kramer and M. Saraceno. *Geometry of the Time- Dependent Variational Principle in Quantum Mechanics.* Ed. Springer-Verlag, Berlin, Vol. 140 (1981).

[37] G. W. Semenoff. *Condensed-Matter Simulation of a Three-Dimensional Anomaly.* Phys. Rev. Lett. ***53***, 2449 (1984).

[38] D. J. Thouless. *Wannier functions for magnetic sub-bands.* J. Phys C ***17***, 12 (1984).

[39] Q. Niu and D. J. Thouless. *Quantized Adiabatic Charge Transport in the Presence of Substrate Disorder and Many-Body Interaction.* J. Phys. A: Math. Gen. ***17***, 2453 (1984).

[40] Q Niu, D. J. Thouless and Y. S. Wu. *Quantized Hall conductance as a topological invariant.* Phys. Rev. B ***31***, 3372 (1985).

[41] R. D. King-Smith and D.Vanderbilt. *Theory of polarization of crystalline solids.* Phys. Rev. B ***47***, 1651(R) (1993).

[42] N. Marzari and D. Vanderbilt. *Maximally localized generalized Wannier functions for composite energy bands.* Phys. Rev. B ***56***, 12847 (1997).

[43] P. Gosselin, F. Ménas, A. Bérard and H. Mohrbach. *Semiclassical dynamics of electrons in magnetic Bloch bands: A Hamiltonian approach.* Europhys. Lett. ***76***, 651 (2006).

[44] B. A. Bernevig and S. C. Zhang. *Quantum Spin Hall Effect.* Phys. Rev. Lett. ***96***, 106802 (2006).

[45] H. Zhang et al. *Topological insulators in $Bi_2Se_3$, $Bi_2Te_3$ and $Sb_2Te_3$ with a single Dirac cone on the surface.* Nature Physics ***5***, 438 (2009).

[46] A. H. Castro Neto et al. *The electronic properties of graphene.* Rev. Mod. Phys. ***81***, 109 (2009).

[47] R. Yu et al. *Equivalent expression of $\mathbb{Z}_2$ topological invariant for band insulators using the non-Abelian Berry connection.* Phys. Rev. B ***84***, 075119 (2011).

[48] H. Weng et al. *Quantum anomalous Hall effect and related topological electronic states.* Advances in Physics ***64***, 3 (2015).

[49] E. I. Blount. *Formalisms of Band Theory.* Solid State Physics ***13***, 305 (1962).

[50] R. A. Bromley, R. B. Murray and A. D. Yoffe. *The band structures of some transition metal dichalcogenides. III. Group VIA: trigonal prism materials.* J. Phys. C ***5***, 759 (1972).

[51] M. Kertesz and R. Hoffmann. *Octahedral vs. trigonal-prismatic coordination and clustering in transition-metal dichalcogenides.* J. Am. Chem. Soc. ***106***, 3453 (1984).

[52] C. M. Goringe, D. R. Bowler and E. Hernández. *Tight-Binding Modelling of Materials.* Reports on Progress in Physics ***60***, 12 (1999).

[53] G. X. Meng and Y. Z. Ping. *Supercell Approach in Tight-Binding Calculation of Si and Ge Nanowire Bandstructures.* Chin. Phys. Lett. ***22***, 2651 (2005).

[54] Z. Y. Zhu, Y. C. Cheng, and U. Schwingenschlögl. *Giant spin-orbit-induced spin splitting in two-dimensional transition-metal dichalcogenide semiconductors.* Phys. Rev. B ***84***, 153402 (2011).

[55] I. Deretzis, G. Calogero, G. G. N. Angilella and A. La Magna. *Role of basis sets on the unfolding of supercell band structures: From tight-binding to density functional theory.* Eur. Phys. Lett. ***107***, 2 (2014).

[56] J. He, K. Hummer and Cesare Franchini. *Stacking effects on the electronic and optical properties of bilayer transition metal dichalcogenides* $MoS_2$ , $MoSe_2$ , $WS_2$ , *and* $WSe_2$. Phys. Rev. B ***89***, 075409 (2014).

[57] A. Kormányos et al. $k \cdot p$ *theory for two-dimensional transition metal dichalcogenide semiconductors.* 2D Materials ***2***, 2 (2015).

[58] A. J. Pearce, E. Mariani and G. Burkard. *Tight-binding approach to strain and curvature in monolayer transition-metal dichalcogenides.* Phys. Rev. B ***94***, 155416 (2016).

[59] Y. Wang et al. *Tight-binding piezoelectric theory and electromechanical coupling correlations for transition metal dichalcogenide monolayers.* Phys. Rev. B ***98***, 125402 (2018).

[60] C. Ataca, H. Şahin and S. Ciraci. *Stable, Single-Layer* $MX_2$ *Transition-Metal Oxides and Dichalcogenides in a Honeycomb-Like Structure.* J. Phys. Chem. C ***116***, 16, 8983 (2012).

[61] A. Vitale et al. *Valleytronics: Opportunities, Challenges, and Paths Forward.* Small ***14***, 1801483 (2018).

[62] O. Gröning et al. *Engineering of robust topological quantum phases in graphene nanoribbons.* Nature ***560***, 209 (2018).

[63] J. Lawrence et al. *Probing the Magnetism of Topological End States in 5-Armchair Graphene Nanoribbons.* ACS Nano. ***14***, 4, 4499 (2020).